Fabrication techniques and applications of two-dimensional photonic crystal: history and the present status

Uttara Biswas,[a] Chittaranjan Nayak,[b] and Jayanta Kumar Rakshit [a,*]

[a]National Institute of Technology Agartala, Department of Electronics and Instrumentation Engineering, Agartala, Tripura, India
[b]Vellore Institute of Technology, School of Electronics Engineering, Department of Communication Engineering, Vellore, Tamil Nadu, India

Abstract. The idea of photonic crystal came to be when E. Yablonovitch and S. John recommended a structure in 1987 having periodic alteration of refractive index in one or multiple directions. Photonic crystals have the potential to manipulate and tailor the flow of light across the crystal, which gives advantage to invent many photonic devices on the microscopic scale having very small footprints. In recent years several articles have been published on the advances of photonic crystal-based structures. This review article mainly focuses on the several fabrication techniques of photonic crystals and their applications in different fields. Several photonic crystal-based structures such as logic gates, optical sensors, polarization beam splitters, and absorbers for solar cells are reviewed in this paper to show recent advancements on this trending topic. Also, a brief review of the different steps of fabrication of photonic crystals and different fabrication methods proposed by researchers is articulated in this paper. © *2022 Society of Photo-Optical Instrumentation Engineers (SPIE)* [DOI: 10.1117/1.OE.62.1.010901]

1 Introduction

The study of light and light-based technological advancement is becoming an economic and social need in the 21st century, and hence photonics is essential to our everyday lives to provide solutions to global challenges in energy, education, agriculture, health, communication, information processing, etc. It goes without saying that photonics has now influenced a wide range of scientific and technological fields, becoming a significant and rapidly evolving area of growing multidisciplinary interest. Medical diagnostics, organic synthesis, communications, and fusion energy are just a few of the many scientific and technical uses for photonics. This can improve people's quality of life across various industries, including advanced manufacturing, military, healthcare, and energy. Today, photonics is also widely employed in agriculture. Without sensors and cameras on tractors and drones, it would be difficult to analyze soil and crops and identify areas that need fertilizer application in precision agriculture. Photonics is also used to predict when and how to harvest crops.

The investigation of the unconventional property of photonic crystal (PhC) with the guiding and confining capability of electromagnetic waves has strengthened the cognizance of the PhC structure. PhCs are the atypical member of the family of optical media having the periodic alteration of the refractive indexes (RIs). The invention of PhC by E. Yablonovitch and S. John in 1987, possessing a periodic structure of dielectric materials and having the ability to guide and confine the electromagnetic waves[1,2] has gained much attention. One of the unique properties of the PhC is the photonic bandgap (PBG), which is created from the destructive interference of the dispersing electromagnetic waves within the PhC. The electromagnetic waves belonging to the

---

*Address all correspondence to Jayanta Kumar Rakshit, jayantarakshit.eie@nita.ac.in

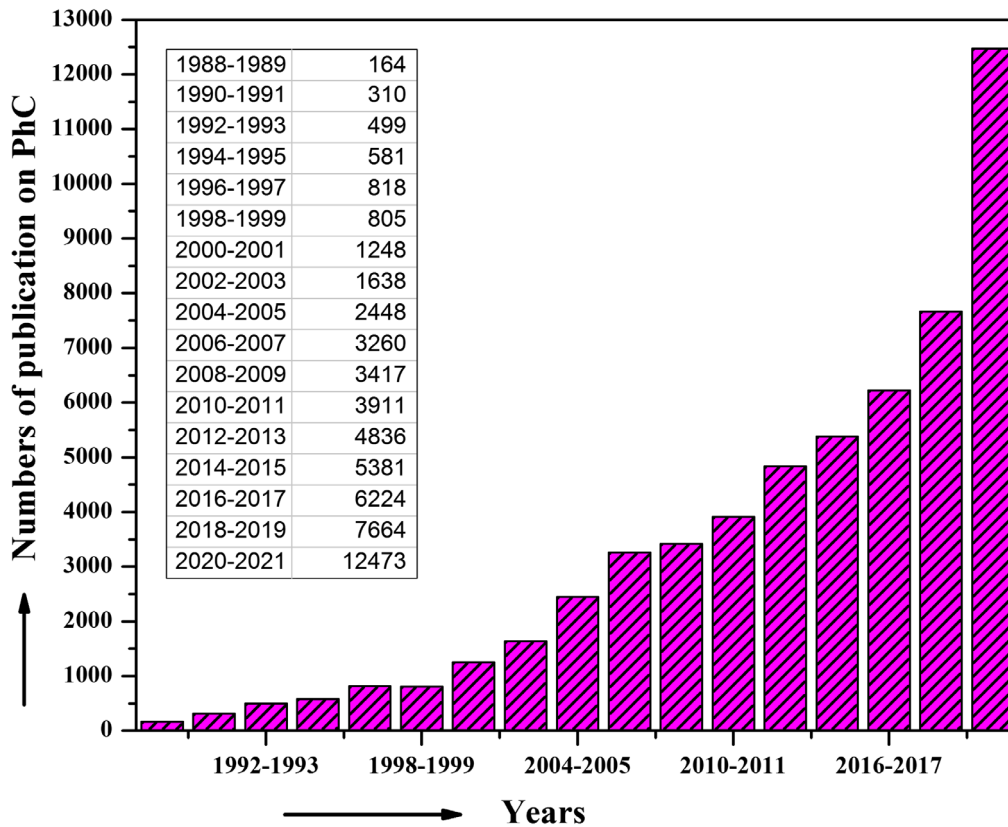| 1988-1989 | 164 |
1990-1991	310
1992-1993	499
1994-1995	581
1996-1997	818
1998-1999	805
2000-2001	1248
2002-2003	1638
2004-2005	2448
2006-2007	3260
2008-2009	3417
2010-2011	3911
2012-2013	4836
2014-2015	5381
2016-2017	6224
2018-2019	7664
2020-2021	12473

Fig. 1 Number of published articles on PhC from the year 1988 to 2021.

frequency bands within PBG are forbidden to pass across the crystal. The property of creating the PBG facilitates the property of manipulation of the electromagnetic waves within the crystal.[3–6] Several conspicuous applications are engaged by the PhCs. Some of the applications are light bending,[7–9] solar cells,[10–13] optical filters,[14–17] optical sensors,[18–21] and many others. The number of scientific publications on PhC is increasing gradually. The number of publications in different scientific journals on PhC-based structures is shown by a bar graph in Fig. 1. From the articles published in the Elsevier journals only, it is seen that the number of articles has a constantly growing trend from 1988 to 2021.[22]

Different geometrical structures of PhCs assort it into three species: one-dimensional (1D) PhC, two-dimensional (2D) PhC, and three-dimensional (3D) PhC. In 1D PhC, RI modulates only in the direction of light propagation and does not change in other directions.[23,24] In 2D PhCs, RI alteration takes place in two directions, and the RI in the third direction remains unchanged.[25,26] Whereas, in 3D PhC, periodic modulation of RI takes place all over three directions.[27,28] All three types of PhCs have their unique applications and are used for different purposes.

After the invention of 1D PhC, it took almost one century to invent the 2D PhC and three years for the 3D PhCs. Though 3D PhCs gained more attention in the earlier days but owing to the relatively easy manufacturing process, 2D PhC, have gained remarkable attention in the current era. Almost all the significant characteristics of PhCs are exhibited in the 2D PhC. Different PhC-based photonic devices can be designed using 2D PhCs for their unique characteristics of non-trivial Brillouin zones and topological sensitivity to a minimum index contrast.[26,29] The electromagnetic field in a 2D periodic media can be classified into two polarization states transverse magnetic (TM) mode and transverse electric (TE) mode. In TM polarization, the magnetic field is polarized along the plane of periodicity, and the electric field is perpendicular to the plane of periodicity. For TE-polarized light, the magnetic field is perpendicular to the plane of periodicity. The introduction of defects in the 2D PhCs has opened up the possibility to engineer spontaneous emission of light from the crystal and thus made it possible to design different photonic devices.

PhC can be used as a photonic reservoir computer on a silicon photonic chip. It shows excellent performance on boolean tasks such as the nonlinear XOR and the AND gate with 25 to 67 Gbps operational speed. Additionally, the exact same reservoir can also perform header recognition for up to six-bit headers.[30] However, one of the main challenges still to overcome is fabricating the reservoir with the correct properties. A high-speed, power-efficient, low-dispersion, and compact electro-optical modulator was also designed using the PhC waveguide.[31] PhC can also be used to fabricate PhC nanocavity lasers with low threshold powers and high-quality factors.[32]

In the first section of this review article, a brief history of PBG materials and the recent advances of PhC-based structures are given. The first section is followed by different fabrication techniques for PhC-based devices in the second section. In the third section, some applications of PhC structures in the fields of optics and photonics are given. The fourth section concludes the article by summarizing all the matters discussed in the earlier sections.

2 Fabrication Technique of Photonic Crystals

Most of the PhC devices proposed in recent years come in the 2D PhC structure and are fabricated in the slab waveguides. Different fabrication techniques of PhC structures have been proposed by different researchers in earlier years.[33–41] Most use silicon-on-insulator (SOI) techniques. Due to the high expenses, the SOI technique is not economically preferable but due to the ease of fabrication using SOI wafers, it is used by many researchers. SOI wafers are advantageous compared to other techniques due to low power consumption as parasitic device capacitance is reduced due to isolation from the bulk silicon substrate and also for higher speed
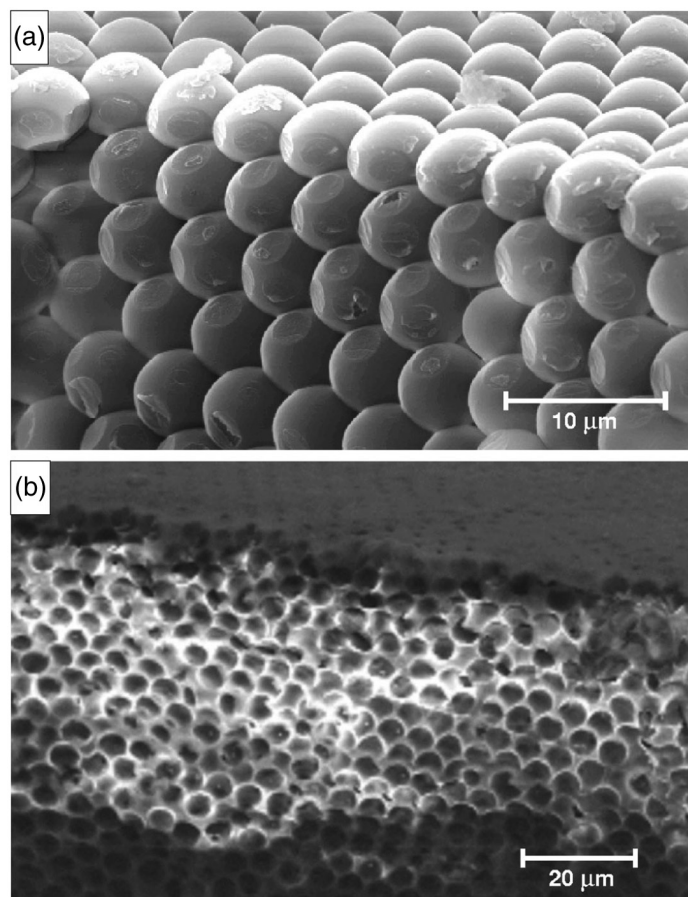
Fig. 2 (a) Cross-sectional scanning electron micrograph image of a sintered opal PhC template fabricated from polystyrene microspheres and (b) cross-sectional image of inverse-opal PhC made from UV-curable poly mer.[44]
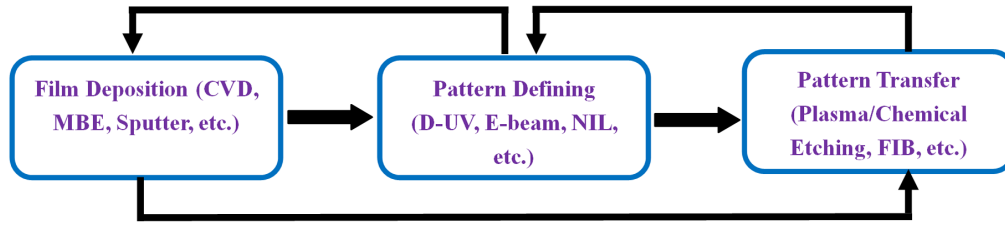
Fig. 3 Fabrication steps of PhC.

of operation.[36,42,43] Chiu et al.[36] fabricated a PhC ring resonator using SOI nano-rods. In another paper, a novel design was proposed for multichannel integrated devices based on SOI PhC concepts and optofluidic technology.[43] Xu et al.[44] proposed a fabrication technique of PhC structures using the combination of centrifugation and spin coating method as shown in Fig. 2

The fabrication technique of PhC mainly includes three steps: film deposition, pattern defining, and pattern transfer as shown in Fig. 3. Some common film deposition techniques are chemical vapor deposition (CVD),[45,46] molecular beam epitaxy (MBE),[47,48] and sputtering.[49] After pattern defining, the sample might have been taken back for deposition purposes in case of metal sputtering in the lift-off method, otherwise, the sample got ready for pattern transfer where various etching techniques such as a plasma or chemical etching and focused ion beam (FIB) etching take place. In the case of FIB, etching as no hard mask is required, so after deposition, the sample is directly transferred for pattern transfer.

2.1 Film Deposition

The thin-film deposition technique mainly includes the processing above the surface of the substrate by adding material to the substrate either in the form of structured layers or as spacers so that later it can be removed.[50,51] Depending on the substrate structure, operating temperature, and rate of deposition chiefly two types of deposition techniques are used namely chemical deposition technique and physical deposition technique. In chemical deposition, a chemical reaction takes place between the hot substrate and inert gases present in the gas chamber at low or atmospheric pressure and thus films are deposited on the substrate.[52] The technique can be further classified into several categories, e.g. CVD, atomic layer deposition (ALD), spin coating, etc. In the case of physical deposition, the raw materials are released and moved physically onto the upper surface of the substrate in the form of a solid, liquid, or vapor. Some common examples of physical deposition are thermal evaporation, MBE, and sputtering. The film deposition process is followed by lithographic techniques to pattern the sample and etching to release the final structure.

2.2 Pattern Defining

To define the desired pattern on the substrate, the lithographic technique is mostly used. Alloys Senefelder invented the lithography technique in 1796.[53,54] Several lithographic techniques used for PhC fabrication are summarized in Table 1 in chronological order.

Table 1 Lithographic techniques used for PhC fabrication.

Sl. No.	Lithographic technique	Year
1	E-beam lithography	1995
2	Deep x-ray lithography	1997
3	Holographic lithography	2000
4	Deep UV lithography	2002
5	Nanoimprint lithography	2007

2.2.1 *Electron-beam lithography (EBL)*

Among the several lithographic techniques, the first lithographic technique for the fabrication of PhC was e-beam lithography, which was used by Cheng and Scherer.[55] Here the combination of wet and dry etching technologies was used to fabricate 3D PBG structures in the optical wavelength range. A hexagonal hole pattern was created on the surface of the sample using electron-beam lithography with a 30 kV incident beam energy. Later, also in 2003, the electron-beam lithography technique was used for structuring 3D self-assembled PhCs.[56] After that, several research papers have been published on PhC fabrication using e-beam lithography.[57–62]

In EBL, a focused beam of electrons is used to pattern a resist layer on the substrate.[63,64] The resist layer is sensitive to electron beam (e-beam) and consists of organic polymer material. Resist can be classified into two types (positive resist and negative resist) depending on the chemical response to the electron exposure (Fig. 4).[65–67] In the case of positive resist, the resist becomes soluble to the resist developer when exposed to the e-beam and in the case of negative resist, the portion of the resist layer becomes insoluble to the resist developer when exposed to the e-beam. The sensitivity of the lithography depends on many factors, such as resist material, the thickness of the resist layer, the substrate material, and also the developer used in the process. E-beam lithography has a higher resolution than photolithography because it is not limited by diffraction and has a very high resolution of nm scale in complex patterns. It also allows multiple designs to be fabricated on a single wafer.

A process of fabrication of defects such as waveguides and resonators embedded in a 3D PhC using EBL was proposed by Murakowski et al.[68] as shown in Fig. 5. Scanning electron micrograph of the 3D PhC is shown in Fig. 6.

2.2.2 *X-ray lithography*

In the x-ray lithography technique, the pattern is defined using a special type of mask with different local x-ray absorption. After being placed on a substrate, this design is reproduced on an x-ray-sensitive substance known as a resist (usually a silicon wafer). Depending on the chemical
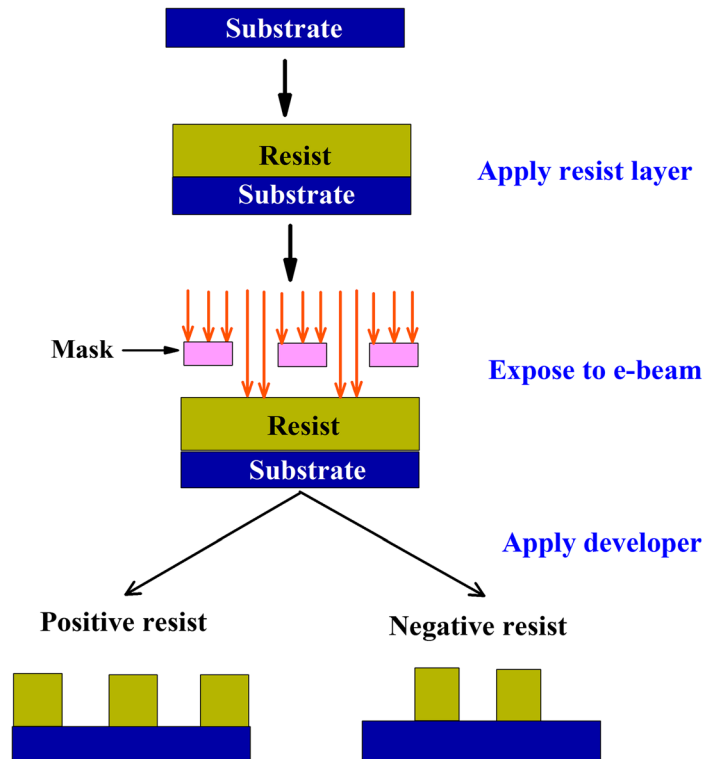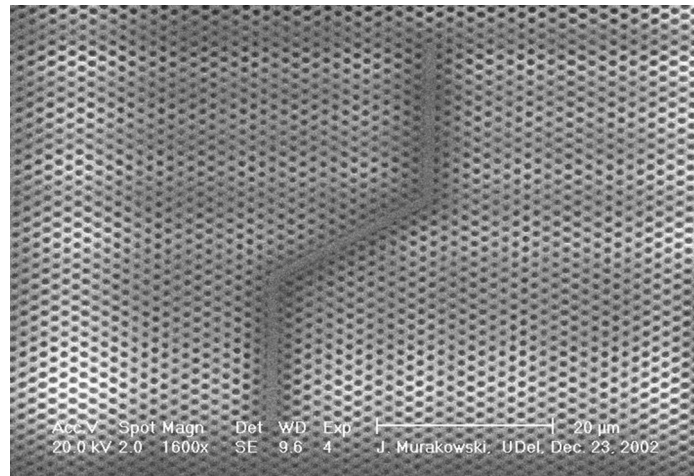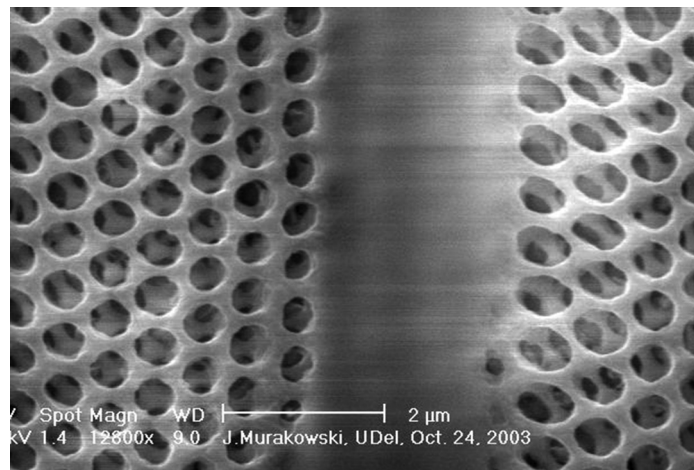

**Fig. 4** Lithography technique with positive and negative resist.[63]

Fig. 5 Waveguide patterned in a 3D PhC.[68]

Fig. 6 Scanning electron micrograph of the 3D PhC.[68]

nature of the resist, cross-linking (for negative resists), or bond breaking (for positive resists) may occur when the x-ray traveling through the pattern strikes the resist. Following exposure, the entire object is submerged in a certain solvent, which, depending on the nature of the solvent, either causes the exposed region to resist to dissolve and produce a pattern or the opposite. The remaining portion of the resistance will remain unaltered. This is how nano-patterns are produced on the substrate via x-ray lithography. The block diagram of the production of nano-patterns is shown in Fig. 7.

In 1997, deep x-ray lithography was used by researchers to fabricate PhC-based devices.[69] Multiple tilted x-ray lithography exposures were used to construct structures with photonic band gaps in the infrared region. In another research paper, three consecutive exposures of polymethyl
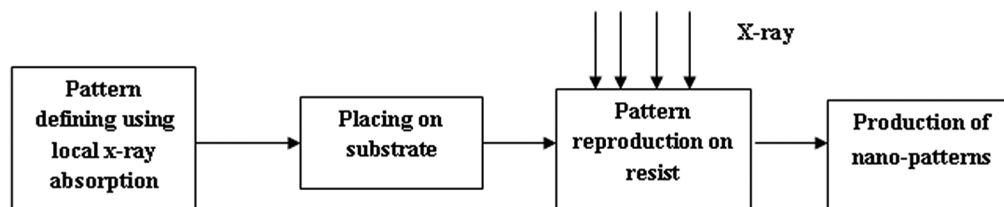
Fig. 7 Block diagram of production of nano-patterns using x-ray lithography.

methacrylate (PMMA) resist were used to an x-ray beam through a triangular lattice of holes.[70] Later, various researchers used deep x-ray lithography to create 2D and 3D PhC.[71,72]

2.2.3 Holographic lithography

Holographic lithography is based on the optical interference of multiple laser beams with a single light exposure. PhC holographic lithography is a fast and low-cost fabrication method that uses an optical field produced by the interference of monochromatic laser beams to expose a photoresist material. The method is composed of two phases, underexposed and overexposed phases after exposure for a period of time. After exposure, a developer material is applied to the photoresist, removing only one of the two phases. The structure that is obtained after the developing step can be used as a model for the creation of PBG materials. The technique has two major advantages over others. It is, first of all, free of masks, inexpensive by nature, and suitable for large-scale PhC production. Second, it is possible to create PhCs with practically any lattice symmetry because there are enough optical factors that can be changed, including beam strength, polarization, and incidence angles. Holographic methods have the advantage of allowing laser light to be directed to any spot or in any pattern without the need for a mechanical stage or photomask. The development of a user-accessible and adaptable instrument is the second focus of this research.

In 2000, holographic lithography was used by Campbell et al.[73] to fabricate the PhC structure. Later, the method was also used by different researchers for the fabrication of PhCs.[74–77]

2.2.4 Photolithography or UV lithography

Photolithography, also known as optical lithography or UV lithography, is a technique for patterning a design on a thin film or bulk of substrate using microfabrication[78–80] In this lithography process, a geometric pattern is transferred by the use of light from an optical mask to a chemical photoresist on the substrate. This method is useful for creating extremely small patterns. The size and shape of the created object can be precisely controlled and also produced in a cost-effective manner. The process also has some drawbacks: a flat substrate is required, and the process is ineffective for creating nonflat shapes; additionally, an extremely clean operating environment is required. The photolithography technique facilitates the smallest feature sizes down to 50 nm.[81,82]

Deep ultraviolet (DUV) photolithography is the process of defining a pattern in a thin photosensitive polymer layer (photoresist) using controlled 254- to 193-nm light such that the resulting polymer pattern can be transferred into or onto the underlying substrate by etching, deposition, or implantation. The exposing light is passed through a chrome-on-quartz photomask, whose opaque areas act as a stencil of the desired pattern.[83,84]

2.2.5 Nanoimprint lithography

Nanoimprint lithography (NIL) is a low-cost, high-resolution pattern fabrication method for nanometer-scale patterns.[85,86] In optical lithographic techniques, photons or electrons are used to draw patterns by modifying the chemical or physical properties of the resist layer. NIL depends on direct mechanical deformation of the resist and can thus attain resolutions above those imposed by light diffraction or beam scattering that are found in standard lithographic techniques. This is in contrast to classic optical lithographic approaches, which build patterns by using photons or electrons to affect the chemical and physical properties of the resist.[85] The smallest size of a template feature that can be manufactured largely determines the resolution of NIL.

2.3 Pattern Transfer

In the pattern transfer technique, the pattern drawn on the resist material through the lithography technique is transferred to the hard mask, usually by the reactive ion etching (RIE) technique, and finally, deep etching is performed using RIE, inductively coupled plasma (ICP) etching, etc.

Etching is a process in which a layer is chemically removed from the surface of a wafer during the manufacturing process. The wafer is immersed in an etching solution and then rinsed clean with hot deionized water. Precautions should be taken so that no etching reactant remains

in the sample after the cleaning process as this may lead to a defective sample. Etching can be further classified into two broad categories: liquid phase or wet etching and plasma phase or dry etching. By monitoring the resistivity of the deionized water, the rinsing time can be determined. If the resistivity of the rinsing water is indifferent to its previous value, then the sample can be considered clean.

Etch rate mainly depends on two factors: saturation of the etchant bath and the chemical concentration. The etch rate can be affected by how long the etchant bath has been sitting, and/or how much material has been etched in the bath. Etch rate and other properties of the etchant depend very strongly on the ratios and concentrations of the chemicals in the etchant.

2.3.1 *Wet etching*

In the case of wet etching, the sample is immersed in a liquid etchant solution to remove or dissolve the material from the substrate. Hydroxides (KOH, CsOH), tetramethylammonium hydroxide, hydrogen fluoride, nitric acid, and acetic acid are some frequently used wet etchants. Several polymers such as polymethyl methacrylate (PMMA), parylene, fluorinated PMMA, poly-Nmethylmethacrylimide (PMMI), etc. are wet etched for the generation of micro-structures.[87,88]

The wet etching processes have high etch rates and are relatively fast. The main equipment for a wet etching process is an etching agent (acids and liquid solvents), immersion tank, or spray system. One of the disadvantages of wet etching is that, because of the isotropic properties of etching, the substrate material both of the bulk wafers and the material under the mask is removed, by the etching chemicals at the same rate. Moreover, a large number of etching chemicals are required for wet etching and so, the chemical and disposal costs related to wet etching are relatively high. Wet etching only needs a container filled with a liquid solution that will dissolve the target substance. Unfortunately, difficulties arise since often a mask is needed to selectively etch the material. A mask that will not disintegrate or at the very least etches much slower than the substance to be patterned is required.

2.3.2 *Dry etching*

In the dry etching or plasma etching process, the substrate material is extracted using plasmas or etchant gases. Dry etching can be further categorized into three types: chemical reactions (by using reactive plasma or gases), physical removal (generally by momentum transfer), and a combination of chemical reactions and physical removal.[89,90] The capability of automation, less material consumption, and the ability to use different gases with no or minimal hardware change are some advantages of dry etching. Dry etching possesses some disadvantages, such as the requirement of a vacuum chamber to operate.

RIE, sputter etching, and vapor phase etching are the three subcategories of the dry etching technique. In RIE, the substrate is put into a reactor that is filled with various gases. An RF power source strikes plasma in the gas mixture, converting the gas molecules into ions. The ions are accelerated toward, and react with, the surface of the material being etched, forming another gaseous material. This is known as the chemical part of RIE. There is also a physical part that is similar in nature to the sputtering deposition process. Without causing a chemical reaction, ions with sufficient energy can knock atoms out of the substance being etched.

Some fabrication methods of PhCs as described by different researchers are narrated in this review article.

2.4 *Etchless Fabrication Method of PhC*

Some researchers demonstrated etchless silicon slab fabrication.[33] The method is followed by two steps; in the first step, a suspended organic membrane is created using direct-write EBL and in the next step, the organic membrane is coated with silicon to create a high contrast of RI.

For the creation of the organic membrane, at first, the substrate material is coated with a thick layer of MMA/MAA copolymer by spinning the liquid solution of the copolymer at a specific speed for a specific time. Then the structure is heated at a specific temperature to evaporate the
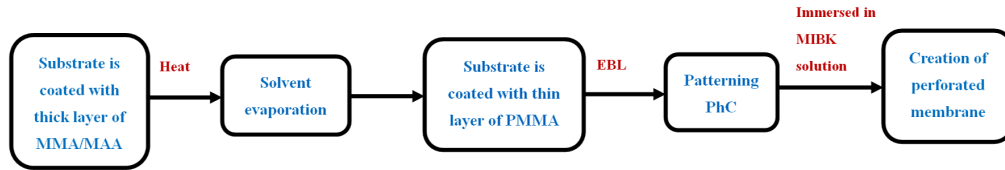
Fig. 8 Steps of etchless fabrication technique of PhC.

solvent. Then again, the silicon substrate is coated with a comparatively thin PMMA layer by spinning the PMMA solution and baking out the solvent at a particular temperature. Now the silicon substrate is coated with copolymer and has the PMMA layer on top. Then the sample is exposed to EBL to pattern the PhC. As both the MAA and PMMA layers are sensitive to e-beam, the electrons can easily perforate through the MAA layer, and the PMMA layer underneath the MAA layer is exposed to the e-beams and thus the polymer chains break due to the interaction with the electrons. So when the sample is immersed in the methyl isobutyl ketone (MIBK) solution, then the regions of the sample exposed to the e-beam dissolve in the solution. As the MAA layer has a higher cessation rate than PMMA, it dissolves faster than PMMA as soon as holes open up in the PMMA layer. As a consequence, an expansive region of MAA is vulnerable to the MIBK solution, The PMMA is undercut, and a suspended perforated membrane is created. Different steps associated with the fabrication technique are described in Fig. 8.

The RI of PMMA is not sufficient to create a sufficient PBG. So in the second step of this fabrication method, silicon is coated on the PMMA membrane by DC sputter coating.

2.5 Suspended PhC Fabrication Using Bulk Wafers

In this process, at first, a layer of silicon oxide is grown-up thermally on the double-side polished single-crystal silicon (SCS) wafer using an oxidation furnace. Then, using photolithography and the lift-off technique, the layer of photoresist is patterned and placed on top of the silicon oxide layer. The subsequent etch in the oxide layer is caused by the photoresist layer. Thus, the required design is transplanted to the oxide layer and consequently on the silicon substrate by dry etching in an RIE system. The thickness of the required PhC slab is determined by the depth of the dry etching. After removing the photoresist layer, the sample is dry oxidized to create a silicon dioxide layer on the sample in order to avoid contamination with the oxidation furnace. After the dry etching is finished, the sample is immersed in a 33% wt KOH solution to release it from the substrate (Fig. 9).

2.6 PhC Fabrication Using SOI Wafers

In this process, an SOI wafer is used as a substrate.[41] The SOI wafer has a silicon layer as a core layer and a thick silicon dioxide (SiO_2) layer as the lower cladding layer. It consists of a single crystal silicon layer placed at the top and separated from the bulk silicon layer by an insulating SiO_2 layer (Fig. 10). At first, using the EBL technique and the ICP etching technique, the upper silicon layer is etched into the lattice of silicon rods. Then a polymer layer is formed among and over the rods, and the polymer has the same RI as the SiO_2 layer. SOI wafers are advantageous compared to other techniques due to their low power consumption, as parasitic device capacitance is reduced due to their isolation from the bulk silicon substrate, and also for their higher speed of operation. Scanning electron microscopic images of the PhC ring resonator are shown
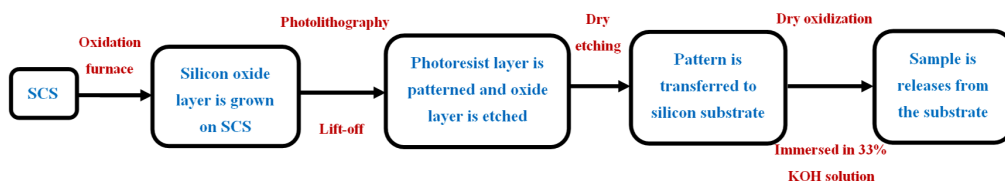

Fig. 9 Steps included in suspended PhC fabrication.
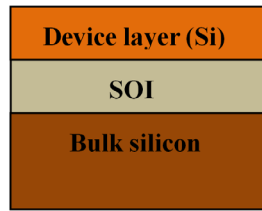
Fig. 10 Schematic diagram of SOI.
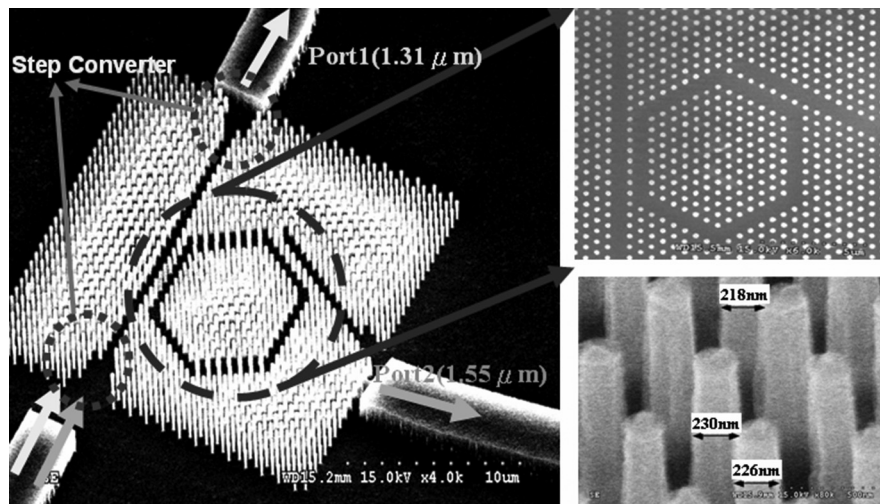
Fig. 11 Scanning electron microscopic images of a PhC ring resonator.[36]
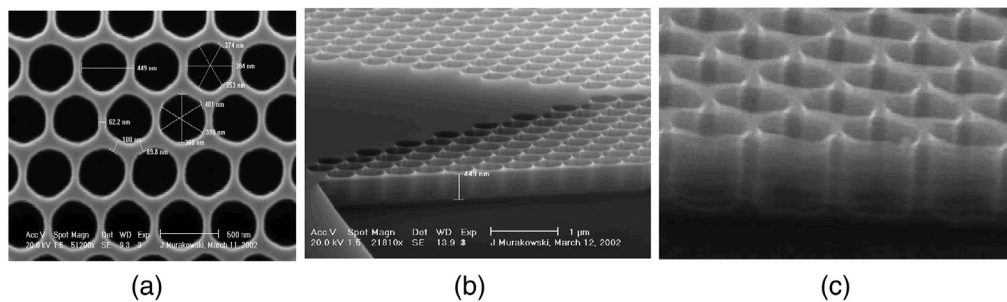
Fig. 12 (a) Top-view, (b) perspective view, and (c) zoom-in view of the fabricated PhC device on SOI wafers.[33]

in Fig. 11.[36] Prather et al.[33] fabricated a 2D PhC device on an SOI wafer. The top-view, perspective view, and zoom-in view of the fabricated device are shown in Fig. 12.

3 Applications of PhC

3.1 *PhC-Based Logic Gates*

PhC-based logic gates are gaining more attention among researchers compared to conventional logic gates due to their compactness, high switching speed, low power consumption, and outstanding integration capabilities into photonic integrated circuits.[91–97] Several logic functions can be accomplished using optical logic gates. The basic requirements for an optical logic gate to be used in integrated circuits are a low delay time, a high contrast ratio, and a small dimension.[98–105]

Table 2 Comparative study of different logic gates proposed in recent years.

| Sl. No.	Reference	Proposed structure	Application	Contrast ratio	Bit rate	Response time	Footprint	Method
1	91	The coupled waveguide in 2D PhC	AND, OR, NOR, NOT	37.7 dB	NM#	NM#	NM#	2D FDTD
2	92	2D PhC structure using kerr effect	XOR, XNOR, NAND, and NOT	20 dB	NM#	0.2 ps	NM#	FDTD
3	93	Use of optical bistability in a 2D PhC	AND gate and majority gate	NM#	500 Gbit/s	2 ps	150 μm^2	FDTD and PWE
4	94	Use of line and point defect in 2D PhC	Comparator circuit	NM#	3.33 Tb/s	NM#	NM#	FDTD
5	95	2D PhC-based nonlinear RR	Half-subtractor	10.31 dB	NM#	Delay time 1.3 ps	610 μm^2	FDTD and PWE
6	96	Cavity structure of PhC	NOR and NAND	NOR: 11.91 dB, NAND: 13.97 dB	NM#	NM#	471.32 μm^2	2D FDTD
7	97	Waveguide based structure of PhC	Different logic gates	5 to 10 dB	0.976 Tb/s	1.024 ps	NM#	FDTD
8	98	PhC structure with line defects	Encoder circuit	16.5 dB	NM#	Delay time <0.1 ps	NM#	FDTD
9	99	PhC structure with line defects	AND, OR, XOR, and NOT	4.77 dB	NM#	NM#	NM#	FDTD
10	100	T-shaped waveguide in PhC	NOT, XOR and XNOR	NOT: 54.83 dB; XOR: 55.23 dB; XNOR: 12.27 dB	NM#	NOT: 0.1256 ps; XOR: 0.136 ps; XNOR: 0.1588 ps	105.75 μm^2 for NOT and XOR	FDTD
11	102	Rod type structure of silicon	Full-subtractor	9.8 dB	294 Gb/s	Rise time and fall time are about 0.9 and 0.7 ps	500 μm^2	FDTD
12	106	PhC structure with line defects	NOT, XOR, and NOR	30 dB	NM#	Power transfer delay 0.1 ps	104.8 μm^2	FDTD
13	107	The square lattice structure of silicon rods	XOR, OR	6.767 dB	Speed 2.5 THz	Delay time 0.4 ps	NM#	FDTD and PWE
14	113	PhC structure with line and point defects	Different logic gates	NM#	1 Tbits/s	1 ps	NM#	PWE
15	114	SOA assisted MZI structure	XOR gate	NM#	160 Gbit/s	NM#	NM#	Simulation

NM#: Not mentioned.

Optical logic gates are a hot area of research as they are the main building block for optical processors. The use of PhC in the optical logic gates has miniaturized the size and enhanced the probability to make integrated optical circuits. PhC-based optical logic gates are advantageous compared to conventional logic gates in terms of their low power consumption (in the order of microwatts) and high switching speed (in the order of femtoseconds) (Table 2).

AND logic gates have found applications in different aspects of the communication field, such as for address recognition, data integrity checking purposes, in the optical oscilloscope, and also for sampling gates. For the assessment of data patterns for address identification, parity checking, data encryption, and decryption purposes, and also for generating pseudorandom patterns, XOR gate is utilized. The main usage of the NOT gate is as an inverter, and the XNOR gate is used for threshold detection purposes.

Several structures have been designed by researchers on PhC to perform different logic operations; such as PhC-based waveguides,[92–94,106,107] microring resonator structures[105,108–110] Mach–Zehnder interferometer structure,[111,112] coupled waveguide-based structure,[91,113] PhC based semiconductor optical amplifier (SOA) structure[114,115] and many others.

Based on the interference effect logic gates can be designed using a liner PhC ring resonator (RR).[105] To design a NOT gate a single RR structure [Fig. 13(a)] and to analyze the NOR gate a cascaded RR structure [Fig. 13(b)] is used in the article. A continuous-wave optical bias signal having an optical power of P_a and wavelength of 1573 nm is used as the reference signal and is continuously given to the structure. If the power received at the output is comparable with P_a then it is considered as "logic 1" and if the output power is zero or very low compared with P_a then the output is considered as "logic 0."

(a)

(b)
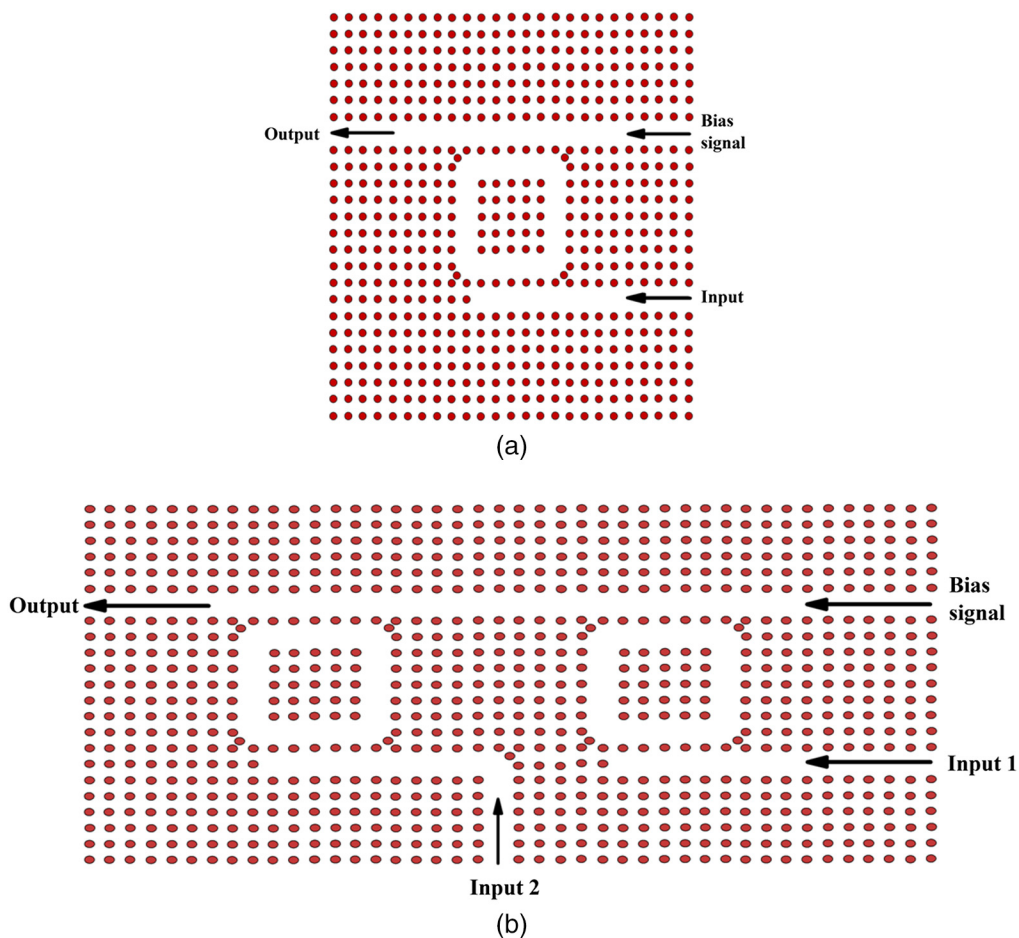
Fig. 13 (a) Single RR structure to attain the NOT gate and (b) cascaded RR structure to attain the NOR gate.[105]

Considering the first structure of PhC [Fig. 13(a)], when no input signal is given to the circuit, then due to the bias signal the optical power received at the output port is $0.85P_a$ which can be considered as "logic 1." If the input signal is given in the circuit, then the input signal destructively interferes with the bias signal at the upper waveguide of the structure and as a result, very low optical power ($0.05P_a$) is received at the output port which is treated as "logic 0." Thus the single RR structure acts as the NOT gate.

Two NOT gates are connected in series to form the NOR gate, as described in Ref. [105] In the cascaded structure, there are two logic input ports "input 1" and "input 2" and one bias signal input. The bias signal has the power of P_a. When both the input signals are absent, then due to the bias signal the output power is $0.6P_a$ which is considered as "logic 1." When either of the two input signals of power P_a is given, then due to destructive interference with the bias input light can not pass to propagate to the output port (output power $0.05P_a$) and remains trapped in the RR. When both the inputs are present, destructive interference occurs in the structure's upper waveguide, and obtained output power is $0.04P_a$ which can be considered as "logic 0."

Sharifi et al.[93] proposed a triangular lattice structure of circular holes in a GaAs substrate to design PhC logic gates using the threshold logic concept.

To analyze the properties of a comparator circuit, a PhC structure was designed and simulated using the hexagonal-type lattice structure of GaAs rods.[94] The proposed optical comparator circuit is very small in size and can be used for very high-speed logic circuits due to a high bit rate of 3.33 Tb/s.

Parandin et al.[106] proposed a simple PhC structure that used line defects and point defects to design three logical gates (NOT, XOR, and NOR). The small dimension, high contrast ratio (30 dB), and low power transfer delay (0.1 ps) of the proposed structure have made it suitable for integrated circuits and high-speed logic circuits.[106]

The nonlinear Kerr effect is also used for designing PhC-based logic circuits. Destructive interference of the input signals and the phase difference caused by different traveling paths are the main concept of the operation of such types of logic circuits.[92] In an article published in 2015, Mohebbi et al. proposed a PhC structure[92] of Si rods along with three rods of the nonlinear Kerr material silicon carbide at the bottom of the bent waveguide. A high contrast ratio of up to 20 dB can be achieved with the proposed structure, which makes it suitable for optical communication and data processing.

PhC plays a crucial role in enhancing the performance and reducing the size of an SOA as PhC has the great confining ability of light. Low absorption loss, less power consumption, and the suppression of undesirable nonlinear effects are the main reasons to prefer the PhC-based SOA over the conventional SOA. By the incorporation of PhC-based SOA in an MZI, the logic operation of OR and AND gates can be implemented.[115] InP (RI = 3.17) is used to make the cladding layers and GaInAsP (RI = 3.47) is used to make the active (core) layer (Fig. 14). The schematic representation of the MZI structure to realize the AND operation is depicted in Fig. 15(a). The data signals used at the input to perform the desired logic operations are Gaussian-shaped and termed as A and B. A data signal (A) and its delayed version are injected in the upper and lower arms of the MZI at a wavelength of λ_A. Another signal B (wavelength of λ_B) given to the middle arm through an optical coupler (OC) is split into two parts with equal intensity and phase and combined with the data signal A and with its delayed version using wavelength selective couplers (WSC) in the upper and lower arms of the MZI and passes through SOA1 and SOA2, respectively. Data signal A and its delayed version create a phase difference and allow B to constructively interfere in the second OC. In the absence of data signal A, no phase difference has occurred and thus the output becomes zero. Only when both the data signals are at logic 1 state, we get the output signal. For the realization of OR gate, A and B and the continuous wave (CW) probe are given to the SOA combined [Fig. 15(b)]. By cross-phase modulation nonlinear effect, a phase difference has occurred in the CW beam in which A and B play a significant role. The CW signal splits into two parts by an OC and is given to the two arms of a delayed interferometer (DI). When both the input signals are absent, then no phase difference is rendered in the CW signal, and as a result, the output is "0" from the DI. Additionally, if any of the data signals A and B or both are present, then the CW acquires the phase change and results in "1" at the DI output. The operation of MZI structures was analyzed at 160 Gb/s.
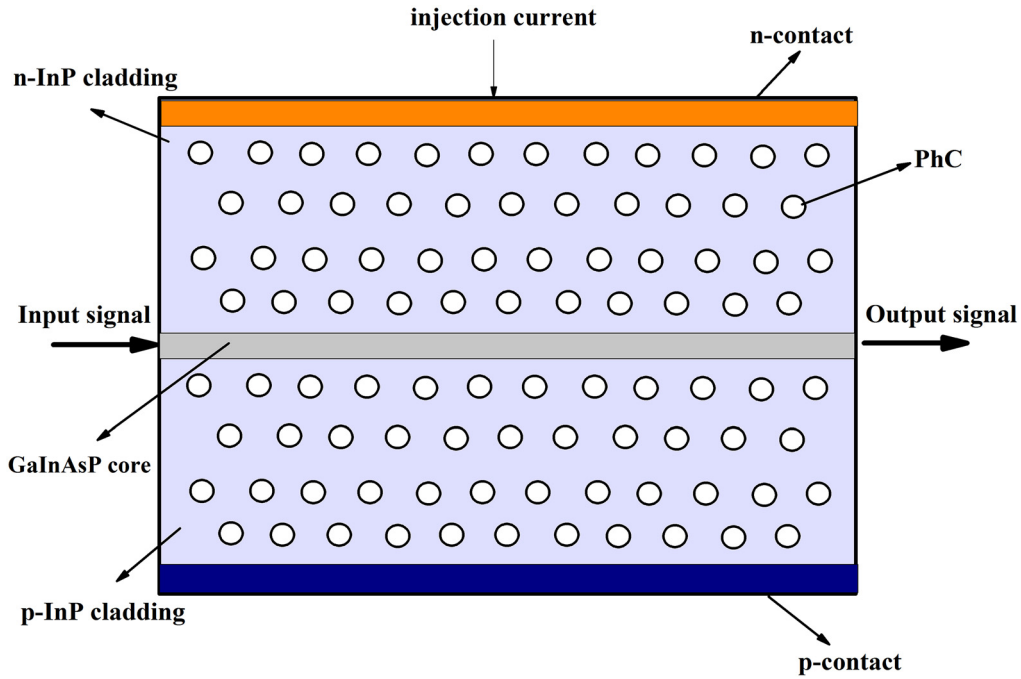
Fig. 14 PhC-based SOA structure.
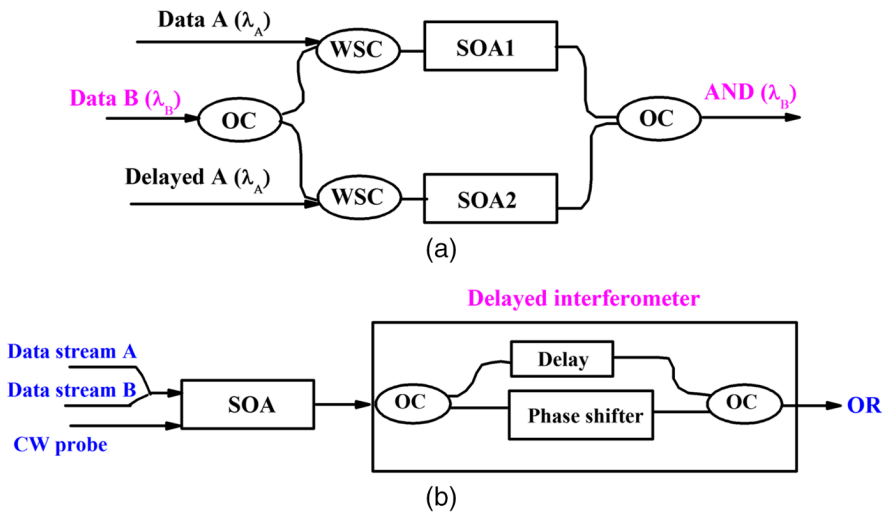
Fig. 15 Schematic representation of MZI structure based on PhC-based SOA to design (a) AND logic gate and (b) OR logic gate.[115]

3.2 PhC-Based Sensors

The growing demand for optical sensing applications has raised the significance of PhC-based optical technologies. Due to the PBG property and the light confinement capability of the PhC-based structures, PhCs and their applications in healthcare,[116–120] RI sensing,[121–124] quality control of food,[125–128] and in many other fields[129–132] is now the sphere of interest for researchers in the present era (Table 3).

Numerous photonic structural designs on various platforms have been extensively researched and used in sensing applications. PhCs provide strong optical confinement to a very tiny volume, enabling the identification of chemical species classified according to their nanoscale size. PhC waveguide components are now being investigated for use in microfluidic and biochemical sensing. Owing to the requirement of minimal sample preparation and high sensitivity, PhC-based RI

Table 3 Comparative study of different sensors proposed in recent years.

Sl. No.	Reference	Proposed structure	Application	Sensor range	Sensitivity	Quality factor	Figure of merit	Resolution	Detection limit	Footprint	Method
1	116	Triangular lattice PCF	RI sensor to detect blood cancer	NM#	8571.43 nm/RIU	NM#	NM#	NM#	NM#	Mesh area 1319 μm^2	FEM
2	117	Nanocavity PhC waveguide	RI sensor to detect different blood components	NM#	Minimum 347.99 nm/RIU	Minimum 3373.2	NM#	NM#	NM#	51.7 μm^2	FDTD and PWE
3	118	Hexagonal shape RR	Biosensor	RI range 1.335–1.341	400 nm/RIU	310	NM#	NM#	NM#	NM#	FDTD
4	119	One dimensional defective PhC structure	Detection of waterborne bacteria	NM#	387.5 nm/RIU	NM#	1174.24 RIU^{-1}	0.0881 nm	2.44×10^{-4} RIU^{-1}	NM#	Simulation
5	121	Plasmonic D-shaped PhC fiber	RI sensor	RI range 1.15–1.36	1700–12600 nm/RIU	NM#	NM#	7.94×10^{-6} RIU	NM#	NM#	FEM
6	122	Birefringent PhC fiber	RI sensor	RI range 1.36–1.41	15428.5 nm/RIU	NM#	NM#	5×10^{-6} RIU	NM#	NM#	FEM
7	123	PhC nanocavity	RI sensor	RI range 1.33–1.45	303.65 nm/RIU	1.38×10^4	357.2 RIU^{-1}	NM#	NM#	NM#	FEM
8	124	PhC waveguide structure with one microcavity	RI sensor	NM#	668 nm/RIU	2×10^6	NM#	NM#	0.002 RIU	NM#	FDTD
9	127	PhC RR structure	RI sensor to analyze different milk constituents	NM#	1 nm/ % of water content, 0.42 nm/% of fat content (1000 nm/RIU)	16857	NM#	NM#	NM#	NM#	FDTD
10	129	PhC microring resonator	Pressure sensor 0–6 MPa	1.37 nm/MPa	26180	NM#	NM#	NM#	NM#	100 μm^2	FDTD and FEM

Table 3 (*Continued*).

| Sl. No.	Reference	Proposed structure	Application	Sensor range	Sensitivity	Quality factor	Figure of merit	Resolution	Detection limit	Footprint	Method
11	130	PCF based Sagnac interferometer	Salinity sensor	Salinity range from 0% to 100%	37,500 nm/RIU and 7.5 nm/% in the salinity range	NM#	NM#	2.66×10^{-6} RIU	NM#	NM#	FEM
12	135	PhC based waveguide with a central defect	Biosensor for RI based cancerous cell detection	NM#	2360.12 nm/RIU	99.765	NM#	1.78×10^{-6} RIU	NM#	NM#	PWE
13	134	PhC based RR	Biosensor for detection of glycated hemoglobin	NM#	690 nm/RIU	2500	1400 RIU^{-1}	NM#	NM#	NM#	FDTD
14	139	Ring shaped cavity RI sensor	RI range 1.33–1.5	536–600 nm/ RIU	1432–2081	737 RIU^{-1}	NM#	1.24×10^{-4} RIU	NM#	NM#	FDTD and PWE
15	142	PhC with linear defects	Gas sensor	NM#	2.3×10^5 nm/RIU	3×10^3	NM#	NM#	NM#	NM#	2.5 var. FDTD
16	144	PhC biperodic waveguide	Optofluidic-gas sensor	1 to 1.5	Gas sensing 610 nm/RIU, Fluid sensing 300 nm/RIU	NM#	NM#	NM#	0.0001 RIU	NM#	FDTD
17	145	PhC Mach–Zehnder interferometer	Pressure sensor	NM#	2.25 nm/MPa	7100	NM#	NM#	873 μPa	400 μm^2	FDTD and FEM
18	146	PhC microcavity coupled to a line defect waveguide	Force sensor	0.25 to 5 GPa	5.82 nm/GPa	NM#	NM#	NM#	NM#	NM#	Experimental

NM#: Not mentioned.

sensors are now extensively investigated by researchers. In the 2D PhC structure, based on the different RI of the analyte samples or owing to changes in the different environmental parameters, the shift in the resonance wavelength takes place and verifying different parameters such as sensitivity, quality factor, the figure of merit, etc. the sensing performance is evaluated. PhC is a nanostructure, which affects the motion of photons within it. The variation in the structural parameters or variation in the analyte samples alters the light-matter interaction within the crystal. As PhCs are periodically modulated structures and create a PBG by forbidding a range of wavelengths to propagate through the crystal, therefore, the localized modes present in the PhC surface can be used for sensing purposes. The RI of the biochemical sample depends on the concentration of the sample and hence the analyte sample can be detected without any modifications by analyzing the light-matter interactions. As the change in the RI of the analyte sample, affects the light confinement properties of the crystal, so by analyzing the confining property of light within the PhC cavity and by optical properties of the PhC structure biochemical sensor can be designed.

A 1D PhC-based sensor was proposed in 2021.[133] Blood plasma and cancer cells can be detected by the introduction of a defect layer sandwiched between two identical 1D PhC structures of silica and titania. The sensitivity of the proposed sensor depends on the thickness of the sample layer. The increase in the sample layer thickness increases the sensitivity of the proposed sensor. By adding an extra layer of SiO_2, on both stacks of PhCs, the sensitivity can be increased without altering the sample layer. By the addition of extra layers of silica, sample thickness can be reduced by 14%. The obtained sensitivity for blood plasma and cancer cells are 72 and 73 nm/RIU, respectively.

A PhC-based biosensor was also investigated which consists of two waveguides critically coupled to a RR.[134] The proposed biosensor is employed for the detection of glycated hemoglobin in human blood. The RR has two single-mode guided waveguides that are critically linked. The bulk sensor is examined in two ways: first, only the silica inside the bore is etched and prepared to be filled with the analyte, and second, the silica from the hub and the bore is etched and prepared to be filled with biomaterial. Here only the background material (silica) is etched, leaving the RR rods in place as shown in Fig. 16. The local RI changes as a result of the binding mechanism between the biomaterial used as the analyte and the cavity or the biorecognition molecules used in the cavity. As a result, the resonance wavelength gets shifted, and employing the FDTD algorithm, the shift in the resonance wavelength and also the quality factors, the figure of merit, changes in the amplitude of the output transmission are analyzed, and consequently, the concentration of glycated hemoglobin is detected.
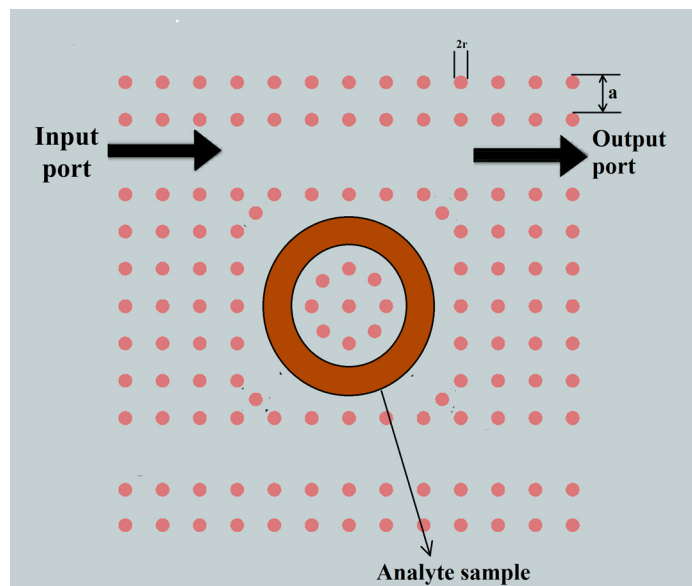
Fig. 16 PhC structure to detect concentration of glycated hemoglobin.

Another novel technique was proposed by Panda and Devi[135] where the differentiation between a normal cell and a cancerous cell is done using a square lattice structure of silicon rods with a central defect. Analyzing the reflected light from the central defect the nature of the cell is detected. The reflected wavelength from normal cells falls under orange-colored wavelength and reflected wavelengths fall under yellow-colored wavelengths. The sensitivity, resolution, and quality factor of the reported sensor were noted as 2360.12 nm/RIU, 1.78×10^{-6}, and 99.765, respectively. It is noted from the investigation that, the cancerous cell has a comparatively higher RI compared with the normal cells due to the fast splitting of cells and because in the cancerous cell more protein particles are absorbed in the cellular organelles.

A 2D hole-type PhC microcavity biosensor was proposed in 2007.[21] The internal surface of the air holes of the sensor is coated with different sizes of protein molecules. In this reported article, the binding of glutaraldehyde and protein molecules creates a monolayer on the surface of the sensor (Fig. 17). Based on the different sizes of protein molecules different amount of resonance redshift occurs, and thus the device performance is analyzed.

In recent years PhC structures are adequately used by researchers for various virus detection purposes.[136–138] Recently, a 1D PhC was proposed by researchers for the detection of the dengue virus. To identify the dengue virus in human, a biosensor has been developed in the recent year.[136] This has been accomplished by using a single defect layer of blood samples (plasma, platelets, and hemoglobin) in a 1D PhC. The defect mode is shifted within a bandgap by the change in RI due to the change of concentration of the blood sample, and this reflects the sensitivity in the event of dengue virus detection.[136] For on-chip and real-time coronavirus detection, a surface plasmon resonance biosensor was investigated by Aliee and Mozafari.[137] In the miniature design, a tiny gold layer is used on the outer layer of an air hole in a photonic quasicrystal fiber with a 12-fold symmetry, allowing the surface plasmon resonance mode on the gold to be excited by leakage of the fiber core mode. The suggested biosensor has a sensitivity of 1172 nm/RIU in the detection of coronaviruses in saliva, according to 3D finite-difference time-domain simulations.

The performance of the optical biosensor is evaluated by testing different parameters such as sensitivity, figure of merit, quality factor, limit of detection, and many others. The most commonly evaluated parameter in the biosensor is sensitivity, which is defined as the smallest change in the resonance wavelength with the change in the RI of the analyte sample and is articulated in nm/RIU. The quality factor is another essential performance parameter for a biosensor and is defined as the ratio of the resonance wavelength to the full-width half maxima of the resonance peak. The high figure of merit of a sensor indicates the high performance of the sensor and is defined as the ratio of the sensitivity to the full-width half maxima. The lowest concentration of analyte sample that can be detected is defined as the limit of detection and a high limit of detection usually enhances the sensitivity.

As the PhC cavities have strong confinement of field and have a long photon lifetime, the resonance wavelength is highly sensitive to perturbation of RI of the infiltrated air holes or the RI of the rods. A PhC nanocavity-based RI sensor was proposed[122] in 2020, coupled with two waveguides, where the resonant peak shifts with the change in the RI.

Another highly sensitive PhC-based RI sensor was proposed[139] incorporating a ring-shaped GaAs cavity. The structure can detect RI from 1.33 to 1.5 and also possesses an excellent figure of merit of 737/RIU.
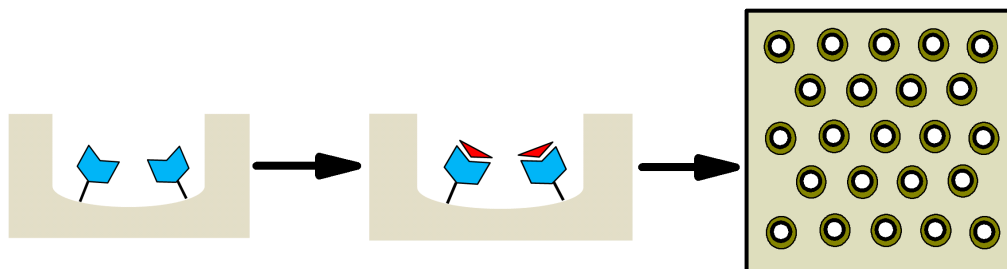
Fig. 17 Creation of monolayer in the internal surface of the sensor.[21]

PhC structures work with only a certain frequency range of light. The light having frequencies that do not fall within PBG cannot pass through the crystal. For variations in temperature, the RI of the material will change which will change the resonance wavelength of the structure. With the increase in temperature for the materials in 2007 having a positive temperature coefficient, RI will increase and will reduce for the materials having a negative temperature coefficient and vice versa. For a temperature sensor, the resonance wavelength gets red-shifted with the increase in material RI and gets blue-shifted with the decrease in material RI.[140,141]

Several PhC-based gas sensors were proposed by different researchers in the earlier years to sense several toxic gases present in the environment such as carbon-di-oxide, methane, carbon-mono-oxide, and many others. Recently, an H_2S gas sensor having high sensitivity and detection limit of 1.2×10^4 nm/RIU and 1.87×10^{-6} RIU, respectively, is reported by researchers.[142] In the proposed sensor air holes are placed on an SOI substrate in a triangular lattice structure. On the inner wall of the cavity, a layer of grapheme is formed so that the gas can be absorbed. When the concentration of the H_2S gas varies, then the RI of the graphene layer also changes ultimately affecting the resonance wavelength of the sensor. The change in the concentration of H_2S gas affects the electrical conductivity of the graphene layer and consequently, the alteration in the RI of the graphene layer takes place which leads to the shift in the resonance wavelength. The resonance wavelength shifts by almost 3.6 nm for a gas concentration change of 1 ppm.

A 2D PhC-based gas sensor was analyzed numerically with three different types of line defects:[143] by removing a row of holes, changing the diameter of a row of holes, and a design with an air channel. The proposed gas sensor works on the principle of transmitting light having a single wavelength from the air holes filled with acetylene gas.

A biperiodic gas sensor was also proposed by researchers[144] for any fluid or gas sensing purpose. The PhC structure consists of a triangular array of air holes with a biperodic structure of waveguide in silicon. Through the biperiodic waveguide, only the resonance wavelengths are allowed to pass; all other wavelengths are reflected back from the crystal. The sensing principle mainly lies in the resonance wavelength shift when the super cavities are filled with some fluid or gas. The proposed sensor is investigated using FDTD analysis. When the cavities are filled with gases, the sensitivity of the proposed sensor is obtained as 610 nm/RIU and the minimum detection limit is 0.0001 RIU. When the structure is used as a fluid sensor, the obtained sensitivity is 300 nm/RIU with an RI detection range of 1.0 to 1.5, and the obtained minimum detection limit is 0.001.

PhC structures can also be realized for mechanical sensing purposes. The PhC structure used for mechanical sensing purposes mainly relies on the photoelastic, piezoelectric, and electro-optic effects of the materials. Due to applied mechanical action, the RI of the materials changes, and also the deformation or deflection of the structure takes place. And as a consequence, the resonance wavelength also shifts to a different wavelength, and by exploiting the shift the applied mechanical actions are realized.

In 2021, PhC based MZI structure was proposed[145] by researchers for pressure sensing purposes. The MZI was integrated onto a silicon diaphragm. The PhC-based MZI consists of two parts: one part is flexible and the other one is a fixed part. As there is no material beneath the flexible portion when pressure is applied to the diaphragm, the flexible part moves downward; RI changes in the flexible arm and thus optical path length is increased in that arm. So light requires comparatively more time to travel in the longer arm compared to the shorter arm due to optical path difference. So the shift in the resonance wavelength takes place whenever pressure is applied to it. Using the finite-element method (FEM) analysis, the applied stress is analyzed, and by using the finite difference time domain (FDTD) method the change in the electromagnetic properties of the interferometer is realized. The pressure sensor has high sensitivity and shows a wavelength resolution of 2.25 nm for 1 MPa applied pressure and possesses a detection limit of the pressure of 873 μPa.

Another force sensor was realized[146] by designing a PhC GaAs/AlGaAs microcavity. In the proposed structure, a microcavity is coupled to a waveguide of the PhC structure which has a triangular lattice of air holes. By removing an air hole and changing the diameters of the surrounding holes, microcavity was created. The structure is feasible in designing PhC actuators where the emission properties of the active PhC can be modulated by the applied strain.

A 2D hexagonal lattice structured PhC design was proposed for pressure sensing purposes in 2019.[147] The structure has the capability of sensing a broad range of pressures, from 20 MPa to 10 GPa. To increase the sensitivity of the structure hexagonal-shaped ring with a hexagonal lattice structure is used. Two silicon cantilever tips are utilized to analyze the applied pressure. The cantilever tips work as the defect in the crystal and with the applied pressure moves downwards and thus the radius of the defect is changed.

3.3 PhC-Based Solar Cells

Thin-film solar cells have attracted many researchers for the low processing temperature and low material consumption. But insufficient absorbance of light in the absorber layer has limited the performance of thin-film solar cells. Also in the case of a silicon wafer, due to an indirect bandgap sufficient light cannot be trapped in the absorber layer. The use of a wavelength-selective medium at the backside of the solar cell can resolve the problem. The absorption is enhanced in the absorber layer of a specially patterned solar cell by increasing the path length of light traveling in the absorber layer. Due to the periodic nanostructure of PhC, they have excellent properties of light trapping, so PhC can be a good choice for thin-film solar cells.[148–153] For light management in a solar cell, 1D PhC structures [distributed Bragg reflector (DBR)], 2D PhC structure [flattened light-scattering substrate (FLiSS)], and the micropyramid structure are used by researchers at the backside of the solar cell.[154] The performance of the solar cell using three types of structures is compared by analyzing the reflectance-transmittance properties using the FDTD simulation method. In the case of DBR, for different layer thicknesses and periods, the performance of the solar cell is analyzed. Different reflectance properties are compared for the different oxide materials in the FliSS structure which has a structurally flat but optically rough surface. In the case of the micro pyramid, structure comparison is done for different heights and with the planar structure. In the PhC structures, enhancement of absorption occurs due to the diffraction effect as the feature size is in the order of the wavelength of light. But in the micropyramid structure, the feature size is greater than the order of the effective wavelength and so enhancement in absorption occurs due to reflection. The reflectance of around 56% is obtained for AZO combined with a hydrogenated amorphous silicon FLiSS structure having a reflectance window ranging from 300 to 720 nm. The micropyramid structure has comparatively less peak reflectance of 40% with the spectral range of reflectance window 300 to 550 nm. Compared with the other two structures, the DBR structure has a high reflectance peak of 75% with a reflectance window from 300 to 650 nm.

Minimizing of surface reflectance is an effective way to increase the efficiency of solar cells. A silicon solar cell without an antireflecting coating reflects almost 40% of the incident light in the surrounding. The inclusion of a single layer of silica can reduce the reflectance by occurring destructive interference between the reflected waves in the surface layers. The use of PhC in photovoltaic devices can increase the absorption rate as PhC has the unique property of trapping light. In an article published in 2021, Mercier et al.[155] proposed a PhC structure superimposed on the top surface of the solar cell to minimize the reflectance losses. The introduction of photonic quasicrystal nanostructuring can reduce effective average reflectance significantly. Though bifacial solar cells have the capability of higher power generation, the problem arises in enhancing their performance due to insufficient infrared absorption. The use of DBR in the backside of solar cells can enhance light absorption in longer wavelengths. For the different bottom angles of the pyramid surface and different thicknesses of the silicon wafer, light absorption at the rear side of the solar cell is analyzed.[156] A reduction in the pyramid bottom angle enhances the light trapping and reaches its maximum at an angle of 20 deg. A comparative study of PhC based solar cells is given in Table 4.

3.4 PhC-Based Beam Power Splitters and Polarizers

In optical communication systems, and photonic integrated circuits, optical beam splitter, and polarization beam splitter are the fundamental component. The optical beam splitter divides the input optical signal into several parts at the output[158–160] whereas the polarization beam splitter (PBS) is used to split the optical signal into two polarization states (TE and TM).[161–163] As the

Table 4 Comparative study of different solar cells proposed in recent years.

Sl. No.	Reference	Proposed structure	Efficiency	Method
1	149	Combination of periodic gratings and DBR in photonic backside texture	20%	Fabrication
2	151	1D PhC used as backside reflectors of solar cell	14.5% for TE mode and 20.01% for TM mode	FDTD and rigorous coupled-wave analysis (RCWA)
3	152	1D PhC used as a broadband dielectric reflector	Absorbance 79.3%	Experimental
4	154	DBR, FLiSS and micro-pyramid structure as backside reflector	Maximum photocurrent 26 mA/cm^2 for FliSS structure	FDTD
5	155	PhC in silicon solar cells	18.1%	FDTD
6	157	PhCs as the light-absorbing layer	22.26% and 26.43% for 2μm and 10 μm thickness of graded-index AR coatings	Theoretical

NM#: Not mentioned.

photonic devices can operate in only one polarization state, therefore, the unpolarized light or light having partial polarization cannot propagate through the device. So, PBS is the most efficient device in photonics to separate the light into two orthogonal states of polarization. To analyze the efficiency of a PBS, polarization extinction ratio (PER) is a vital figure of merit[164,165] and is the indicator of the degree of polarization for a polarization-maintaining device.

Small footprints of PhC-based PBS have made it more attractive among researchers.[166–170] The combined effect of self-collimation and PBG is utilized in Ref. 170 to achieve two orthogonal states of polarization of light. Self-collimation in a PhC structure allows light with a particular state of polarization to pass through it in a straight line without any diffraction. To separate different polarized light, a heterostructure of PhC is used. Two structures of a PhC having rectangular air holes (PhC2) and circular air holes (PhC1) are inclined at an angle of the 45-deg interface (Fig. 18). Two outputs have been obtained at the two ports placed at the end of two different types of PhC structures (PhC1 and PhC2). Due to PBG, PhC2 does not allow
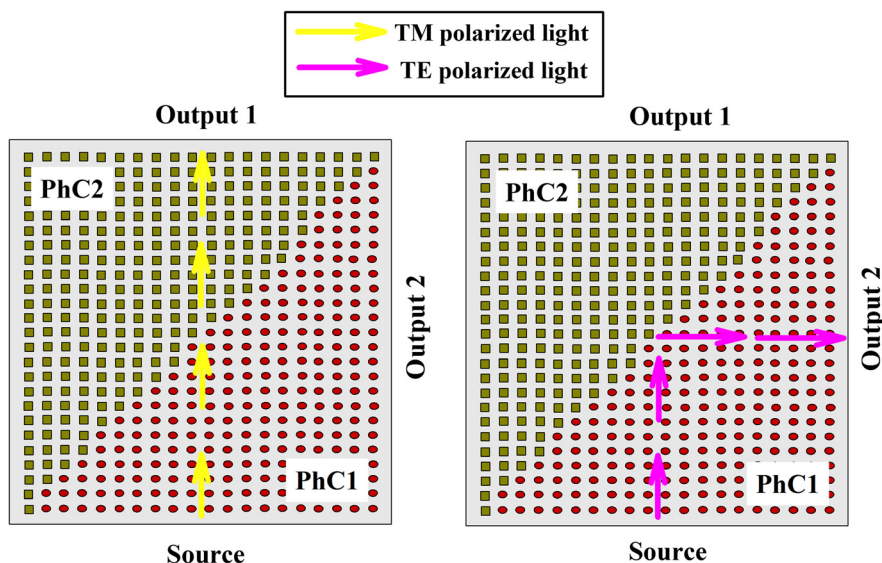
Fig. 18 PhC heterostructure to design a PBS.[170]

TE-polarized light to pass through it and allows only TM-polarized light. On the other hand, Both TE and TM polarized light can pass through the PhC1. The source is placed at one end of the PhC1. When self-collimated TE polarized light is incident from the source, then after passing through the PhC1 it strikes at the interface of the two PhC structures and then reflected with a 90° bend, and output is received at output 2. When self-collimated TM polarized light has emerged from the source, then after marginal refraction at the interface, the light passes through the PhC2, and output is received at output 1. In the self-collimation wavelength interval of 1500 to 1615 nm, transmissivity is about 60% and 78% for TE and TM polarized input light. Additionally, at the wavelength of 1550 nm, the transmissivity is increased and reached up to 94.9% and 88% with high PER of 17 and 41 dB for TE and TM polarized light.

Unlike conventional optical fiber, photonic crystal fiber (PCF) cladding comprises periodically arranged air holes and attracts researchers for its endlessly single-mode guiding operation, high nonlinear effect, low loss, and the controllability of dispersion. The surface plasmon resonance (SPR) effect is also utilized in PCF by different researchers to design PBS.[171,172] In a PCF, air holes of the cladding are filled with metal nanowires to enhance the SPR effect.[171] The light having two polarization states can be filtered out at two communication bands. At the resonance wavelength of 1.24 μm, confinement loss is 10738.726 and 272.2325 dB/m for x and y polarization, respectively. Also, the obtained crosstalks are -90.9 and 85 dB for x and y polarizations at resonance wavelengths of 1.24 and 1.32 μm, respectively.

In Ref. 172, a novel PCF is designed based on SPR to be used as a polarization filter. Some air holes are selectively coated with a gold layer and filled with water. The peak loss obtained for the polarization filter in the direction of y-polarization is 1209.57 dB/cm at 1310 nm wavelength whereas for the x-polarization peak loss is almost zero. The position and the intensity of the loss peak can also be varied by changing the air hole diameter and the metal layer thickness.

A PBS is designed in the THz region is designed based on 2D PhC cavities.[173] PhC line defects and two PhC cavities are combined to design the PBS, which can separate the TE and TM polarized light into two propagation directions in the THz wave frequency ranging from 1.16 to 1.19 THz (Fig. 19). In the THz wave region, Tellurium has a very negligible absorption and for this reason, a square lattice structure of Tellurium rods is used to design the PBS. The internal PhC section is highly transmissive for TM mode but highly reflective for TE mode. A Gaussian shape pulse source (TE/TM) of center frequency $0.236(a/\lambda)$ when inserted at the input port, then the light having TE polarization reflected back from the internal section of the PhC structure with high reflection efficiency, and the output is collected at output A. But the light having TM polarization transmits through the PhC internal section with high transmission efficiency and is finally collected at output B (Fig. 19). The obtained extinction ratio is larger than 20 dB for both TE and TM polarization. A comparative study of different PhC based PBS is given in Table 5.

4 Discussion

Many advances have been made in the past few decades toward the fabrication of high-quality PhCs in large-area for various emerging applications, including metamaterials, sensing, displays, drug screening, and bio-medical applications.[177] Although the research in the quality of PhCs has been optimized in recent years, the complexity of the material fabrication process has progressively increased. Nevertheless, these technologies to fabricate high-quality PhCs still need to be further developed before they can be widely used for various practical applications. Research is
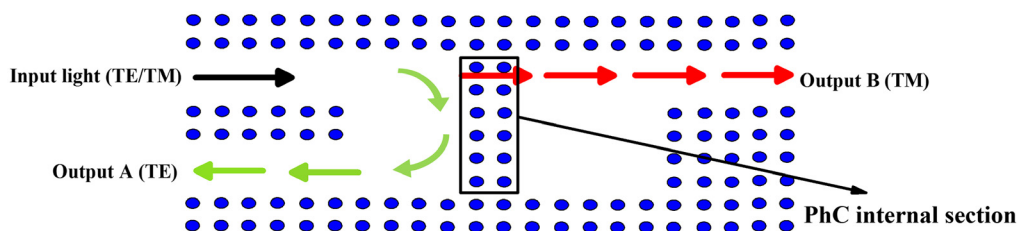

Fig. 19 PhC structure for PBS in THz region.[173]

Table 5 Comparative study of different PBS proposed in recent years.

Sl. No.	Reference	Proposed structure	Polarization extinction ratio	Transmission	Method
1	160	Nonchannel dispersion guiding structure and a beam-splitting structure	NM#	Output power 85%	Fabrication
2	166	GaS chalcogenide dual-core PCF	104 dB	NM#	FEM
3	167	Octagonal PCF PBS with gold-plated film	−151.43 dB	NM#	FEM
4	169	Dispersion-based PhC structure	NM#	85%	FDTD
5	170	Silicon PhC heterostructure	13 and 31 dB for TE and TM polarization at 1150 nm bandwidth; 7 and 41 dB for TE and TM polarization at 1550 nm	60% and 78% for TE and TM polarization at 1150 nm bandwidth; 94.9% and 88% for TE and TM polarization at 1550 nm	FDTD
6	173	PhC structure with line defects	Larger than 20 dB	NM#	FDTD
7	174	PhC directional coupler with triangular lattice structure of air holes	20 dB	NM#	FDTD
8	175	Self-collimating PhC structure	NM#	35% for TM and 30% for TE polarized light	Experimental
9	176	PBS based on the phenomenon of a PhC directional coupler	24.56 and 28.29 dB for TE and TM polarization	NM#	FDTD

NM#: Not mentioned.

currently being conducted for the improvement of external efficiency of LED using PhC. The semiconductor is still invariably used as an active material for the fabrication of LEDs, which is the most efficient light-generating material known, with up to 99.7% internal quantum efficiency reported.[178] But the main problem lies in the extraction of this light. As a consequence of Snell's law, only the radiation within a small cone can escape, everything else being totally internally reflected.[179] The propagation loss of PhCs is the combination of absorbance loss and scattering loss. To reduce the propagation loss in PhC, the ratio of the radius of the rod to the lattice constant (r/a ratio) should be properly optimized. A low propagation loss of 11 dB/mm was reported in a 2D PhC waveguides.[180] The propagation loss of 4 dB/mm was reported in PhC waveguides.[181]

PhCs can also be used for the design of laser cavities as the PhCs have the ability to lower the threshold of semiconductor lasers. This is a very desirable prospect, because one of the major hurdles for working toward denser photonic integration of the removal of excess heat generated by the finite laser threshold.

5 Conclusion

After providing a brief introduction to PhC and PhC-based structures, several fabrication techniques of PhC-based devices are discussed in this review article. Three fabrication steps associated with the fabrication method (film deposition, pattern defining, and pattern transfer) are demonstrated in this review article. Later, the fabrication techniques are followed by different

applications of PhC-based structures such as PhC-based logic gates, PhC-based optical sensors, polarization beam power splitters, polarizers, and also the absorber of solar cells based on PhC structures. Due to the PBG properties of PhC structures, the manipulation of the electromagnetic waves is possible, and also the light confinement capability becomes the key feature of these types of structures. The compactness, high switching speed, low power consumption, and outstanding integration capability of PhC-based logic gates have made them more attractive among researchers. In the case of optical sensors, minimal sample requirements, small footprints, high sensitivity, and high-quality factors are the key advantages of PhC structures. As the PBG property increases the light confinement ability so the use of PhC structures in the absorbers of solar cells increases the efficiency of the solar cell.

A further condition is that the difference between the low index and the high index regions should be large enough for a PBG to appear. This limits the range of materials that can be used. Although the research in the quality of PhCs has been optimized in recent years, the complexity of the material fabrication process has progressively increased. Nevertheless, these technologies to fabricate high-quality PhCs still need to be further developed before they can be widely used for various practical applications.

In the future, PhC-based 3D/4D printing could be promising to fabricate on-demand photonic structures for optics, sensing, displays, biomedical, environmental, safety, and other applications. The 3D PhCs are still far from commercialization but may put forward added features such as optical nonlinearity required for the operation of optical transistors used in optical computers.

Acknowledgments

References

1. E. Yablonovitch, "Inhibited spontaneous emission in solid-state physics and electronics," *Phys. Rev. Lett.* **58**(20), 2059 (1987).
2. S. John, "Strong localization of photons in certain disordered dielectric superlattices," *Phys. Rev. Lett.* **58**(23), 2486 (1987).
3. J. D. Joannopoulos et al., *Molding the Flow of Light*, Princeton University Press, Princeton, New Jeresy (2008).
4. E. Yablonovitch, "Photonic band-gap structures," *J. Opt. Soc. Am. B* **10**(2), 283–295 (1993).
5. M. Scalora et al., "Transparent, metallo-dielectric, one-dimensional, photonic band-gap structures," *J. Appl. Phys.* **83**(5), 2377–2383 (1998).
6. A. Moroz, "Three-dimensional complete photonic-band-gap structures in the visible," *Phys. Rev. Lett.* **83**(25), 5274 (1999).
7. S. Yamada et al., "Observation of light propagation in two-dimensional photonic crystal-based bent optical waveguides," *J. Appl. Phys.* **89**(2), 855–858 (2001).
8. T. Baba, N. Fukaya, and J. Yonekura, "Observation of light propagation in photonic crystal optical waveguides with bends," *Electron. Lett.* **35**(8), 654–655 (1999).
9. Y. Zhang and B. Li, "Photonic crystal-based bending waveguides for optical interconnections," *Opt. Express* **14**(12), 5723–5732 (2006).
10. S. Guldin et al., "Dye-sensitized solar cell based on a three-dimensional photonic crystal," *Nano Lett.* **10**(7), 2303–2309 (2010).
11. M. Florescu et al., "Improving solar cell efficiency using photonic band-gap materials," *Sol. Energy Mater. Sol. Cells* **91**(17), 1599–1610 (2007).
12. B. Curtin, R. Biswas, and V. Dalal, "Photonic crystal based back reflectors for light management and enhanced absorption in amorphous silicon solar cells," *Appl. Phys. Lett.* **95**(23), 231102 (2009).

13. X. Lu et al., "A low-cost high-efficiency crystalline silicon solar cell based on one-dimensional photonic crystal front surface textures," *J. Opt.* **15**(7), 075705 (2013).

14. M. Arjmand et al., "Optical filter based on photonic crystal resonant cavity," *Optoelectron. Adv. Mater. Rapid Commun.* **9**, 32–35 (2015).

15. R. Sathyadevaki et al., "Photonic crystal-based optical filter: a brief investigation," *Photonic Network Commun.* **33**(1), 77–84 (2017).

16. G. Rajalakshmi, A. S. Raja, and D. Shanmuga Sundar, "Design and optimization of two dimensional photonic crystal based optical filter," *J. Nonlinear Opt. Phys. Mater.* **24**(03), 1550027 (2015).

17. A. Vaisi, M. Soroosh, and A. Mahmoudi, "Low loss and high-quality factor optical filter using photonic crystal-based resonant cavity," *J. Opt. Commun.* **39**(3), 285–288 (2018).

18. S. K. Vijaya and S. Robinson, "Two-dimensional photonic crystal based sensor for pressure sensing," *Photonic Sens.* **4**(3), 248–253.

19. S. Sen, M. Abdullah-Al-Shafi, and M. A. Kabir, "Hexagonal photonic crystal fiber (H-PCF) based optical sensor with high relative sensitivity and low confinement loss for terahertz (Thz) regime," *Sens. Bio-Sens. Res.* **30**, 100377 (2020).

20. Y. Liu and H. W. M. Salemink, "Photonic crystal-based all-optical on-chip sensor," *Opt. Express* **20**(18), 19912–19920 (2012).

21. M. Lee and P. M. Fauchet, "Two-dimensional silicon photonic crystal based biosensing platform for protein detection," *Opt. Express* **15**(8), 4530–4535 (2007).

22. https://www.sciencedirect.com/search?qs=photonic%20crystal

23. L.-G. Wang, H. Chen, and S.-Y. Zhu, "Omnidirectional gap and defect mode of one-dimensional photonic crystals with single-negative materials," *Phys. Rev. B* **70**(24), 245102 (2004).

24. S. Colodrero, M. Ocaña, and H. Míguez, "Nanoparticle-based one-dimensional photonic crystals," *Langmuir* **24**(9), 4430–4434 (2008).

25. H. Benisty et al., "Optical and confinement properties of two-dimensional photonic crystals," *J. Lightwave Technol.* **17**(11), 2063–2077 (1999).

26. D. N. Chigrin et al., "Self-guiding in two-dimensional photonic crystals," *Opt. Express* **11**(10), 1203–1211 (2003).

27. J. H. Moon and S. Yang, "Chemical aspects of three-dimensional photonic crystals," *Chem. Rev.* **110**(1), 547–574 (2010).

28. K. Ishizaki and S. Noda, "Manipulation of photons at the surface of three-dimensional photonic crystals," *Nature* **460**(7253), 367–370 (2009).

29. S. Nojima and Y. Kamakura, "Irreducible first brillouin-zone for two-dimensional binary-compound photonic crystals," *J. Phys. Soc. Jpn.* **77**(3), 034403 (2008).

30. F. Laporte et al., "Numerical demonstration of neuromorphic computing with photonic crystal cavities," *Opt. Express* **26**(7), 7955–7964 (2018).

31. X. Zhang et al., "High performance optical modulator based on electro-optic polymer filled silicon slot photonic crystal waveguide," *J. Lightwave Technol.* **34**(12), 2941–2951 (2016).

32. M. Lončar and Y. Qiu, "Low-threshold photonic crystal laser," *Appl. Phys. Lett.* **81**(15), 2680–2682 (2002).

33. D. W. Prather et al., "Novel fabrication methods for 2D photonic crystals in silicon slab waveguides," *Proc. SPIE* **4984**, 89–99 (2003).

34. S. Assefa et al., "Fabrication of photonic crystal waveguides composed of a square lattice of dielectric rods," *J Vac. Sci. Technol. B: Microelectron. Nanometer Struct. Process. Meas. Phenom.* **22**(6), 3363–3365 (2004).

35. S. Assefa et al., "Guiding 1.5μm light in photonic crystals based on dielectric rods," *Appl. Phys. Lett.* **85**(25), 6110–6112 (2004).

36. W.-Y. Chiu et al., "A photonic crystal ring resonator formed by SOI nano-rods," *Opt. Express* **15**(23), 15500–15506 (2007).

37. X. Meng et al., "Design and fabrication of photonic crystals in epitaxial free silicon for ultrathin solar cells," in *Asia Commun. and Photonics Conf. and Exhibit. (ACP)*, IEEE, pp. 1–7 (2011).

38. R. De Ridder et al., "Fabrication of photonic crystal slabs and defects using laser interference lithography and focused ion beam-assisted deposition," in *Proc. 2002 4th Int. Conf. Transp. Opt. Networks (IEEE Cat. No. 02EX551)*, IEEE, Vol. 2, pp. 14–19 (2002).

39. M. Lončar et al., "Design and fabrication of silicon photonic crystal optical waveguides," *J. Lightwave Technol.* **18**(10), 1402 (2000).

40. L. Pang, W. Nakagawa, and Y. Fainman, "Fabrication of two-dimensional photonic crystals with controlled defects by use of multiple exposures and direct write," *Appl. Opt.* **42**(27), 5450–5456 (2003).

41. M. Tokushima, H. Yamada, and Y. Arakawa, "1.5-μm-wavelength light guiding in waveguides in square-lattice-of-rod photonic crystal slab," *Appl. Phys. Lett.* **84**(21), 4298–4300 (2004).

42. G. K. Celler and S. Cristoloveanu, "Frontiers of silicon-on-insulator," *J. Appl. Phys.* **93**(9), 4955–4978 (2003).

43. J. Faneca et al., "One-dimensional multi-channel photonic crystal resonators based on silicon-on-insulator with high quality factor," *Front. Phys.* **6**, 33 (2018).

44. Y. Xu et al., "Centrifugation and spin-coating method for fabrication of three-dimensional opal and inverse-opal structures as photonic crystal devices," *J. Micro/Nanolithogr. MEMS MOEMS* **3**(1), 168–173 (2004).

45. M. Duneau, F. Delyon, and M. Audier, "Holographic method for a direct growth of three-dimensional photonic crystals by chemical vapor deposition," *J. Appl. Phys.* **96**(5), 2428–2436 (2004).

46. H. Miguez et al., "Photonic bandgap engineering in germanium inverse opals by chemical vapor deposition," *Adv. Mater.* **13**(21), 1634–1637 (2001).

47. M. Nishimoto et al., "Air-hole retained growth by molecular beam epitaxy for fabricating gaas-based photonic-crystal lasers," *Appl. Phys. Express* **6**(4), 042002 (2013).

48. J. Heo, W. Guo, and P. Bhattacharya, "Monolithic single gan nanowire laser with photonic crystal microcavity on silicon," *Appl. Phys. Lett.* **98**(2), 021110 (2011).

49. F. Scotognella et al., "Metal oxide one dimensional photonic crystals made by rf sputtering and spin coating," *Ceram. Int.* **41**(7), 8655–8659 (2015).

50. N. Y. Abu-Thabit and A. S. H. Makhlouf, "Fundamental of smart coatings and thin films: Synthesis, deposition methods, and industrial applications," in *Advances in Smart Coatings and Thin Films for Future Industrial and Biomedical Engineering Applications*, A. S. H. Makhlouf and N. Y. Abu-Thabit, Eds., pp. 3–35, Elsevier (2020).

51. M. Summers and M. Brett, "Optimization of periodic column growth in glancing angle deposition for photonic crystal fabrication," *Nanotechnology* **19**(41), 415203 (2008).

52. N. Tétreault et al., "Dielectric planar defects in colloidal photonic crystal films," *Adv. Mater.* **16**(4), 346–349 (2004).

53. F. Hua et al., "Patterning of layer-by-layer self-assembled multiple types of nanoparticle thin films by lithographic technique," *Nano Lett.* **2**(11), 1219–1222 (2002).

54. H. Chik and J. M. Xu, "Nanometric superlattices: non-lithographic fabrication, materials, and prospects," *Mater. Sci. Eng.: R: Rep.* **43**(4), 103–138 (2004).

55. C.-C. Cheng and A. Scherer, "Fabrication of photonic band-gap crystals," *J. Vac. Sci. Technol. B: Microelectron. Nanometer Struct. Process. Meas. Phenom.* **13**(6), 2696–2700 (1995).

56. P. Ferrand et al., "Structuring of self-assembled three-dimensional photonic crystals by direct electron-beam lithography," *Appl. Phys. Lett.* **83**(25), 5289–5291 (2003).

57. G. Subramania and S. Lin, "Fabrication of three-dimensional photonic crystal with alignment based on electron beam lithography," *Appl. Phys. Lett.* **85**(21), 5037–5039 (2004).

58. Y. Ruan et al., "Fabrication of high-q chalcogenide photonic crystal resonators by e-beam lithography," *Appl. Phys. Lett.* **90**(7), 071102 (2007).

59. J. Stodolka et al., "Fabrication of two-dimensional hybrid photonic crystals utilizing electron beam lithography," *Microelectron. Eng.* **78**, 442–447 (2005).

60. Y. Khan et al., "Fabrication and investigation of spectral properties of a dielectric slab waveguide photonic crystal based fano-filter," *Crystals* **12**(2), 226 (2022).

61. A. S. Baburin et al., "Highly directional plasmonic nanolaser based on high-performance noble metal film photonic crystal," *Proc. SPIE* **10672**, 106724D (2018).

62. J. Li et al., "Low loss propagation in slow light photonic crystal waveguides at group indices up to 60," *Photonics Nanostruct. Fundam. Appl.* **10**(4), 589–593 (2012).

63. A. A. Tseng et al., "Electron beam lithography in nanoscale fabrication: recent development," *IEEE Trans. Electron. Packag. Manuf.* **26**(2), 141–149 (2003).

64. M. Altissimo, "E-beam lithography for micro-/nanofabrication," *Biomicrofluidics* **4**(2), 026503 (2010).

65. D. V. Nicolau et al., "Negative and positive tone protein patterning on e-beam/deep-uv resists," *Langmuir* **15**(11), 3845–3851 (1999).

66. H. Yang et al., "Comparative study of e-beam resist processes at different development temperature," *Microelectron. Eng.* **84**(5–8), 1109–1112 (2007).

67. S. Tedesco et al., "Resist processes for hybrid (electron-beam/deep ultraviolet) lithography," *J. Vac. Sci. Technol. B: Microelectron. Nanometer Struct. Process. Meas. Phenom.* **16**(6), 3676–3683 (1998).

68. J. Murakowski et al., "Fabrication of 3D photonic crystals with embedded defects," *Proc. SPIE* **5347**, 181–189 (2003).

69. G. Feiertag et al., "Fabrication of photonic crystals by deep x-ray lithography," *Appl. Phys. Lett.* **71**(11), 1441–1443 (1997).

70. C. Cuisin et al., "Fabrication of three-dimensional photonic structures with submicrometer resolution by x-ray lithography," *J. Vac. Sci. Technol. B: Microelectron. Nanometer Struct. Process., Meas. Phenom.* **18**(6), 3505–3509 (2000).

71. F. Romanato et al., "Fabrication by means of x-ray lithography of two-dimensional GaAs/ALGaAs photonic crystals with an unconventional unit cell," *Nanotechnology* **13**(5), 644 (2002).

72. F. Romanato et al., "Fabrication of 3D metallic photonic crystals by x-ray lithography," *Microelectron. Eng.* **67**, 479–486 (2003).

73. M. Campbell et al., "Fabrication of photonic crystals for the visible spectrum by holographic lithography," *Nature* **404**(6773), 53–56 (2000).

74. D. N. Sharp et al., "Photonic crystals for the visible spectrum by holographic lithography," *Opt. Quantum Electron.* **34**(1), 3–12 (2002).

75. L. Wu et al., "Fabrication of large area two-and three-dimensional polymer photonic crystals using single refracting prism holographic lithography," *Appl. Phys. Lett.* **86**(24), 241102 (2005).

76. S.-G. Park et al., "Cu$_2$o inverse woodpile photonic crystals by prism holographic lithography and electrodeposition," *Adv. Mater.* **23**(24), 2749–2752 (2011).

77. T. Kondo et al., "Holographic lithography of periodic two-and three-dimensional microstructures in photoresist su-8," *Opt. Express* **14**(17), 7943–7953 (2006).

78. M. D. Levenson, N. S. Viswanathan, and R. A. Simpson, "Improving resolution in photolithography with a phase-shifting mask," *IEEE Trans. Electron Devices* **29**(12), 1828–1836 (1982).

79. W. J. Kim and D. L. Trumper, "High-precision magnetic levitation stage for photolithography," *Precis. Eng.* **22**(2), 66–77 (1998).

80. A. Revzin et al., "Fabrication of poly (ethylene glycol) hydrogel microstructures using photolithography," *Langmuir* **17**(18), 5440–5447 (2001).

81. K. Anselme et al., "The interaction of cells and bacteria with surfaces structured at the nanometre scale," *Acta Biomater.* **6**, 3824–3846 (2010).

82. D. B. Miller et al., "Super-resolved critical dimensions in far-field i-line photolithography," *J. Micro/Nanolithogr. MEMS MOEMS* **18**(1), 013505 (2019).

83. W. Bogaerts et al., "Fabrication of photonic crystals in silicon-on-insulator using 248-nm deep UV lithography," *IEEE J. Sel. Top. Quantum Electron.* **8**(4), 928–934 (2002).

84. L. A. Woldering et al., "P made in silicon with reactive ion etching and deep UV lithography," *Nanotechnology* **19**(14), 145304 (2008).

85. L. J. Guo, "Nanoimprint lithography: methods and material requirements," *Adv. Mater.* **19**(4), 495–513 (2007).

86. S. Y. Chou et al., "Sub-10 nm imprint lithography and applications," *J. Vac. Sci. Technol. B: Microelectron. Nanometer Struct. Process. Meas. Phenom.* **15**(6), 2897–2904 (1997).

87. B. Balakrisnan, S. Patil, and E. Smela, "Patterning PDMS using a combination of wet and dry etching," *J. Micromech. Microeng.* **19**(4), 047002 (2009).

88. C. Wochnowski et al., "Femtosecond-laser-assisted wet chemical etching of polymer materials," *J. Appl. Polym. Sci.* **100**(2), 1229–1238 (2006).

89. K. Nojiri, *Dry etching Technology for Semiconductors*, Springer (2015).

90. J. Garra et al., "Dry etching of polydimethylsiloxane for microfluidic systems," *J. Vac. Sci. Technol. A: Vac. Surf. Films* **20**(3), 975–982 (2002).

91. W. Belhadj, N. Saidani, and F. Abdelmalek, "All-optical logic gates based on coupled heterostructure waveguides in two dimensional photonic crystals," *Optik* **168**, 237–243 (2018).

92. Z. Mohebbi, N. Nozhat, and F. Emami, "High contrast all-optical logic gates based on 2D nonlinear photonic crystal," *Opt. Commun.* **355**, 130–136 (2015).

93. H. Sharifi, S. M. Hamidi, and K. Navi, "A new design procedure for all-optical photonic crystal logic gates and functions based on threshold logic," *Opt. Commun.* **370**, 231–238 (2016).

94. F. Parandin, "Ultra-compact terahertz all-optical logic comparator on GaAs photonic crystal platform," *Opt. Laser Technol.* **144**, 107399 (2021).

95. A. Askarian, "Design and analysis of all optical half subtractor in 2D photonic crystal platform," *Optik* **228**, 166126 (2021).

96. A. Kumar and S. Medhekar, "All optical nor and nand gates using four circular cavities created in 2D nonlinear photonic crystal," *Opt. Laser Technol.* **123**, 105910 (2020).

97. P. Rani, Y. Kalra, and R. Sinha, "Design of all optical logic gates in photonic crystal waveguides," *Optik* **126**(9-10), 950–955 (2015).

98. F. Parandin, "High contrast ratio all-optical 4×2 encoder based on two-dimensional photonic crystals," *Opt. Laser Technol.* **113**, 447–452 (2019).

99. K. Fasihi, "Design and simulation of linear logic gates in the two-dimensional square-lattice photonic crystals," *Optik* **127**(11), 4669–4674 (2016).

100. E. H. Shaik and N. Rangaswamy, "Realization of xnor logic function with all-optical high contrast xor and not gates," *Opto-Electron. Rev.* **26**(1), 63–72 (2018).

101. A. Askarian, G. Akbarizadeh, and M. Fartash, "An all-optical half subtractor based on Kerr effect and photonic crystals," *Optik* **207**, 164424 (2020).

102. N. Khajeheian et al., "An all optical full subtractor based on nonlinear photonic crystals," *Optik* **245**, 167751 (2021).

103. F. Parandin and M. Moayed, "Designing and simulation of 3-input majority gate based on two-dimensional photonic crystals," *Optik* **216**, 164930 (2020).

104. Y. Fu, X. Hu, and Q. Gong, "Silicon photonic crystal all-optical logic gates," *Phys. Lett. A* **377**(3-4), 329–333 (2013).

105. A. Kumar and S. Medhekar, "All optical not and nor gates using interference in the structures based on 2D linear photonic crystal ring resonator," *Optik* **179**, 237–243 (2019).

106. F. Parandin et al., "Reconfigurable all-optical not, xor, and nor logic gates based on two dimensional photonic crystals," *Superlattices Microstruct.* **113**, 737–744 (2018).

107. K. Goudarzi et al., "All-optical xor and or logic gates based on line and point defects in 2-D photonic crystal," *Opt. Laser Technol.* **78**, 139–142 (2016).

108. C. Kumar et al., "Design of photonic crystal or gate with multi-input processing capability on a single structure," *Mater. Today:. Proc.* **47**, 1586–1589 (2021).

109. S. Sadegh-Bonab and H. Alipour-Banaei, "A novel proposal for an all-optical 2-bit adder/subtractor based on photonic crystal ring resonators," *Photonics Nanostruct. Fundam. Appl.* **39**, 100777 (2020).

110. H. Alipour-Banaei, S. Serajmohammadi, and F. Mehdizadeh, "All optical nand gate based on nonlinear photonic crystal ring resonators," *Optik* **130**, 1214–1221 (2017).

111. D. Correia et al., "Obtaining optical logic gates–or, xor, and and logic functions using asymmetric Mach-Zehnder interferometer based on photonic crystal fiber," *Opt. Laser Technol.* **97**, 370–378 (2017).

112. M. M. Gupta and S. Medhekar, "All-optical not and and gates using counter propagating beams in nonlinear Mach–Zehnder interferometer made of photonic crystal waveguides," *Optik* **127**(3), 1221–1228 (2016).

113. H. Sharifi, S. M. Hamidi, and K. Navi, "All-optical photonic crystal logic gates using nonlinear directional coupler," *Photonics Nanostruct. Fundam. Appl.* **27**, 55–63 (2017).

114. A. Kotb and K. E. Zoiros, "Performance analysis of all-optical xor gate with photonic crystal semiconductor optical amplifier-assisted Mach–Zehnder interferometer at 160 gb/s," *Opt. Commun.* **402**, 511–517 (2017).

115. A. Kotb, K. E. Zoiros, and C. Guo, "Ultrafast performance of all-optical and and or logic operations at 160 gb/s using photonic crystal semiconductor optical amplifier," *Opt. Laser Technol.* **119**, 105611 (2019).

116. M. A. Mollah et al., "Twin core photonic crystal fiber refractive index sensor for early detection of blood cancer," *Sens. Bio-Sens. Res.* **29**, 100344 (2020).

117. N. A. Mohammed et al., "High-sensitivity ultra-quality factor and remarkable compact blood components biomedical sensor based on nanocavity coupled photonic crystal," *Results Phys.* **14**, 102478 (2019).

118. P. Yashaswini, H. Gayathri, and P. Srikanth, "Performance analysis of photonic crystal based biosensor for the detection of bio-molecules in urine and blood," *Mater. Today:. Proc.* (2021).

119. A. Panda and P. D. Pukhrambam, "Investigation of defect based 1D photonic crystal structure for real-time detection of waterborne bacteria," *Physica B* **607**, 412854 (2021).

120. T. Endo et al., "Reflectometric detection of influenza virus in human saliva using nanoimprint lithography-based flexible two-dimensional photonic crystal biosensor," *Sens. Actuators, B* **148**(1), 269–276 (2010).

121. W. Zeng, Q. Wang, and L. Xu, "Plasmonic refractive index sensor based on d-shaped photonic crystal fiber for wider range of refractive index detection," *Optik* **223**, 165463 (2020).

122. S. Das and V. K. Singh, "Refractive index sensor based on selectively liquid infiltrated birefringent photonic crystal fiber," *Optik* **201**, 163489 (2020).

123. C. Qi et al., "Refractive index sensor based on photonic crystal nanocavity," *Opt. Commun.* **464**, 125393 (2020).

124. M. Ammari, F. Hobar, and M. Bouchemat, "Photonic crystal microcavity as a highly sensitive platform for RI detection," *Chin. J. Phys.* **56**(4), 1415–1419 (2018).

125. S. M. Atiqullah et al., "Detection of harmful food additives using highly sensitive photonic crystal fiber," *Sens. Bio-Sens. Res.* **23**, 100275 (2019).

126. A. Malinin et al., "Photonic crystal fibers for food quality analysis," *Proc. SPIE* **8427**, 842746 (2012).

127. U. Biswas, J. K. Rakshit, and G. K. Bharti, "Design of photonic crystal microring resonator based all-optical refractive-index sensor for analyzing different milk constituents," *Opt. Quantum Electron.* **52**(1), 1–15 (2020).

128. U. Biswas, G. K. Bharti, and J. K. Rakshit, "Design of photonic crystal based optical sensor for analyzing water content in milk," in *Intelligent Techniques and Applications in Science and Technology*, S. Dawn et al., Eds., Springer, pp. 143–149 (2019).

129. V. R. Kolli et al., "A high q-factor photonic crystal microring-resonator based pressure sensor," *Photonics Nanostruct. Fundam. Appl.* **43**, 100870 (2021).

130. M. A. Mollah et al., "Highly sensitive photonic crystal fiber salinity sensor based on sagnac interferometer," *Results Phys.* **16**, 103022 (2020).

131. K. Zhan et al., "Enhanced-performance relative humidity sensor based on MOF-801 photonic crystals," *Phys. Lett. A* **384**(26), 126678 (2020).

132. G. Fu et al., "Temperature insensitive curvature sensor based on cascading photonic crystal fiber," *Opt. Fiber Technol.* **41**, 64–68 (2018).

133. A. Bijalwan, B. K. Singh, and V. Rastogi, "Analysis of one-dimensional photonic crystal based sensor for detection of blood plasma and cancer cells," *Optik* **226**, 165994 (2021).

134. A. Tavousi, M. R. Rakhshani, and M. A. Mansouri-Birjandi, "High sensitivity label-free refractometer based biosensor applicable to glycated hemoglobin detection in human blood using all-circular photonic crystal ring resonators," *Opt. Commun.* **429**, 166–174 (2018).

135. A. Panda and P. P. Devi, "Photonic crystal biosensor for refractive index based cancerous cell detection," *Opt. Fiber Technol.* **54**, 102123 (2020).

136. S. Sharma and A. Kumar, "Design of a biosensor for the detection of dengue virus using 1D photonic crystals," *Plasmonics* **17**(2), 675–680 (2022).

137. M. Aliee and M. H. Mozaffari, "Photonic quasi-crystal fiber-based plasmonic biosensor: a platform for detection of coronavirus," *Plasmonics* **17**, 1655–1660 (2022).

138. N. Joshi, S. Shukla, and R. J. Narayan, "Novel photonic methods for diagnosis of sars-cov-2 infection," *Transl. Biophotonics* **4**, e202200001 (2022).

139. F. Rahman-Zadeh, M. Danaie, and H. Kaatuzian, "Design of a highly sensitive photonic crystal refractive index sensor incorporating ring-shaped GaAs cavity," *Opto-Electron. Rev.* **27**(4), 369–377 (2019).

140. U. Biswas et al., "Design of an ultra-compact and highly-sensitive temperature sensor using photonic crystal based single micro-ring resonator and cascaded micro-ring resonator," *Silicon* **13**(3), 885–892 (2021).

141. Y. Peng et al., "Temperature sensor based on surface plasmon resonance within selectively coated photonic crystal fiber," *Appl. Opt.* **51**(26), 6361–6367 (2012).

142. A. Afsari, M. J. Sarraf, and F. Khatib, "Application of tungsten oxide thin film in the photonic crystal cavity for hydrogen sulfide gas sensing," *Optik* **227**, 165664 (2021).

143. A. Zakrzewski and S. Patela, "Modelling of a two-dimensional photonic crystal with line defect for a laser gas sensor application," *Opto-Electron. Rev.* **25**(2), 80–88 (2017).

144. A. Kumar, T. S. Saini, and R. K. Sinha, "Design and analysis of photonic crystal biperiodic waveguide structure based optofluidic-gas sensor," *Optik* **126**(24), 5172–5175 (2015).

145. V. R. Kolli et al., "A high sensitive photonic crystal Mach-Zehnder-interferometer based pressure-sensor," *Results Opt.* **5**, 100118 (2021).

146. T. Stomeo et al., "Fabrication of force sensors based on two-dimensional photonic crystal technology," *Microelectron. Eng.* **84**(5-8), 1450–1453 (2007).

147. R. Ghosh, K. Ghosh, and R. Chakraborty, "High resolution wide range pressure sensor using hexagonal ring and micromachined cantilever tips on 2D silicon photonic crystal," *Opt. Commun.* **431**, 93–100 (2019).

148. S. P. Sreenilayam et al., "Photonic crystals-based light-trapping approach in solar cells," in *Nano-Optics*, S. Thomas et al., Eds., pp. 337–345, Elsevier (2020).

149. X. Sheng, L. Z. Broderick, and L. C. Kimerling, "Photonic crystal structures for light trapping in thin-film si solar cells: Modeling, process and optimizations," *Opt. Commun.* **314**, 41–47 (2014).

150. J. Krügener et al., "Photonic crystals for highly efficient silicon single junction solar cells," *Sol. Energy Mater. Sol. Cells* **233**, 111337 (2021).

151. S. Saravanan and R. Dubey, "Light-harvesting enhancement in ultrathin film silicon solar cells using photonic and plasmonic nanostructures," *Mater. Today:. Proc.* **50**(1), 85–89 (2022).

152. A. Soman and A. Antony, "Tuneable and spectrally selective broadband reflector–modulated photonic crystals and its application in solar cells," *Sol. Energy* **162**, 525–532 (2018).

153. M. Guo et al., "Coupling plasmonic nanoparticles with tio_2 nanotube photonic crystals for enhanced dye-sensitized solar cells performance," *Electrochim. Acta* **263**, 373–381 (2018).

154. M. S. Uddin, C. Vijayan, and J. Rath, "Optical modelling of photonic and geometrical structures used for light management in thin-film solar cells," *Mater. Today Proc.* **39**, 1974–1977 (2021).

155. T. M. Mercier et al., "High symmetry nano-photonic quasi-crystals providing novel light management in silicon solar cells," *Nano Energy* **84**, 105874 (2021).

156. J. Wang et al., "Benefits of photonic management strategy for highly efficient bifacial solar cells," *Opt. Commun.* **462**, 125358 (2020).

157. A. Chutinan, N. P. Kherani, and S. Zukotynski, "High-efficiency photonic crystal solar cell architecture," *Opt. Express* **17**(11), 8871–8878 (2009).

158. N. Kazanskiy and R. Skidanov, "Binary beam splitter," *Appl. Opt.* **51**(14), 2672–2677 (2012).

159. Y. Xiao et al., "Slow light beam splitter," *Phys. Rev. Lett.* **101**(4), 043601 (2008).

160. S. Shi et al., "Dispersion-based beam splitter in photonic crystals," *Opt. Lett.* **29**(6), 617–619 (2004).

161. N. Zhao et al., "Broadband polarization beam splitter by using cascaded tapered bent directional couplers," *IEEE Photonics J.* **11**(4), 1–8 (2019).

162. L.-M. Chang et al., "Polarization-independent directional coupler and polarization beam splitter based on asymmetric cross-slot waveguides," *Appl. Opt.* **57**(4), 678–683 (2018).

163. Z. Yi-Fan et al., "Heterojunction polarization beam splitter based on self-collimation in photonic crystal," *Acta Phys. Sin.* **67**(3), 034204 (2018).

164. K. Zhou et al., "High extinction ratio in-fiber polarizers based on 45 tilted fiber bragg gratings," *Opt. Lett.* **30**(11), 1285–1287 (2005).

165. J. Liu et al., "Method for improving the polarization extinction ratio of multifunction integrated optic circuits," *Opt. Express* **29**(18), 28096–28103 (2021).

166. G.-M. Zheng, "Mid-infrared broadband polarization beam splitter based on gas photonic crystal fiber with high extinction ratio," *Optik* **241**, 166971 (2021).

167. J. Lou, T. Cheng, and S. Li, "Ultra-short polarization beam splitter with square lattice and gold film based on dual-core photonic crystal fiber," *Optik* **179**, 128–134 (2019).

168. X. Chen et al., "Polarization beam splitter based on photonic crystal self-collimation Mach–Zehnder interferometer," *Opt. Commun.* **284**(1), 490–493 (2011).

169. X. Shen et al., "Dispersion-based all photonic crystals polarization beam splitter," *Phys. Lett. A* **369**(5-6), 524–527 (2007).

170. D. Liu, D. Citrin, and S. Hu, "Compact high-performance polarization beam splitter based on a silicon photonic crystal heterojunction," *Opt. Mater.* **109**, 110256 (2020).

171. J. Qin et al., "Surface plasmon enhanced polarization filter of high birefringence photonic crystal fiber with a partial core based on filled silver nanowire," *Opt. Fiber Technol.* **60**, 102342 (2020).

172. X. Yan et al., "A novel gold-coated PDF polarization filter based on surface plasmon resonance," *Opt. Laser Technol.* **126**, 106125 (2020).

173. J.-S. Li and H. Liu, "Terahertz polarization beam splitter based on two photonic crystal cavities," *Optik* **126**(1), 139–143 (2015).

174. T. Liu et al., "Design of a compact photonic-crystal-based polarizing beam splitter," *IEEE Photonics Technol. Lett.* **17**(7), 1435–1437 (2005).

175. V. Zabelin et al., "Self-collimating photonic crystal polarization beam splitter," *Opt. Lett.* **32**(5), 530–532 (2007).

176. P. Rani, Y. Kalra, and R. K. Sinha, "Complete photonic bandgap-based polarization splitter on silicon-on-insulator platform," *J. Nanophotonics* **10**(2), 026023 (2016).

177. Z. Cai et al., "From colloidal particles to photonic crystals: advances in self-assembly and their emerging applications," *Chem. Soc. Rev.* **50**(10), 5898–5951 (2021).

178. I. Schnitzer et al., "Ultrahigh spontaneous emission quantum efficiency, 99.7% internally and 72% externally, from ALGaAs/GaAs/ALGaAs double heterostructures," *Appl. Phys. Lett.* **62**(2), 131–133 (1993).

179. T. F. Krauss and M. Richard, "Photonic crystals in the optical regime—past, present and future," *Prog. Quantum Electron.* **23**(2), 51–96 (1999).

180. A. Talneau, L. Le Gouezigou, and N. Bouadma, "Quantitative measurement of low propagation losses at 1.55μm on planar photonic crystal waveguides," *Opt. Lett.* **26**(16), 1259–1261 (2001).

181. J. Arentoft et al., "Low-loss silicon-on-insulator photonic crystal waveguides," *Electron. Lett.* **38**(6), 1 (2002).

Uttara Biswas received her MTech in electrical engineering from the National Institute of Technology Agartala, India, in 2018 and she is currently pursuing her PhD in the Department of Electronics and Instrumentation Engineering at the National Institute of Technology Agartala, Agartala, India. Her current research interests include photonics and photonic crystal-based structures.

Chittaranjan Nayak received his PhD in engineering from the National Institute of Technology Agartala, Agartala, India, in 2017. He is currently working as an associate professor in the Department of Communication Engineering, Vellore Institute of Technology, Vellore, India. His current research interests include soft computing, photonic multilayers, and the formation of photonic nanojets for different optoelectronic applications.

Jayanta Kumar Rakshit received his BTech and MTech degrees from the University of Calcutta, India, in 2002 and 2004, respectively. He received his PhD in engineering from National Institute of Technology Agartala, Agartala, India, in 2015. He is presently working as an assistant professor in the Department of Electronics and Instrumentation Engineering at National Institute of Technology Agartala, an Institute of National Importance in India. His current research interests include photonics, optical sensors, optical logic-based signal processing, optical computing, and optical communication. He has published/accepted more than 66 papers in international/national journals/symposia proceedings. He has guided two scholars for their PhD thesis. He is senior member of Institute of Electrical and Electronics Engineers (IEEE) and Life member of Optical Society of India (OSI).